

Article

Transformation of the Sub-Continental Lithospheric Mantle Beneath the North China Craton (NCC): Constraints from the Geochemical Characteristics of Olivine Websterite Xenoliths and Their Minerals in the Cenozoic Basalts from Hannuoba

Xianzhe Duan ^{1,2}, Hongjie Shen ^{1,2,3}, Nan Li ², Wenzhou Xiao ^{1,2}, Qinglin Sui ^{1,2}, Haiyang He ^{1,2}, Peng Feng ^{1,2,*} and Zhenping Tang ^{2,*}

¹ School of Resource & Environment and Safety Engineering, University of South China, Hengyang 421001, China; 2014000504@usc.edu.cn (X.D.); 205011007@csu.edu.cn (H.S.); lilzhou@usc.edu.cn (W.X.); 2021000069@usc.edu.cn (Q.S.); hehy@usc.edu.cn (H.H.)

² Hunan Key Laboratory of the Rare Metal Minerals Exploitation and Geological Disposal of Wastes, Hengyang 421001, China; 2014000420@usc.edu.cn

³ School of Geosciences and Info-Physics, Central South University, Changsha 410083, China

* Correspondence: fengpeng@usc.edu.cn (P.F.); tangzhenping@usc.edu.cn (Z.T.)



Citation: Duan, X.; Shen, H.; Li, N.; Xiao, W.; Sui, Q.; He, H.; Feng, P.; Tang, Z. Transformation of the Sub-Continental Lithospheric Mantle Beneath the North China Craton (NCC): Constraints from the Geochemical Characteristics of Olivine Websterite Xenoliths and Their Minerals in the Cenozoic Basalts from Hannuoba. *Minerals* **2022**, *12*, 401. <https://doi.org/10.3390/min12040401>

Academic Editors: Magdalena Dumańska-Słowik, Beata Naglik, Giovanni Ruggieri and Tomasz Toboła

Received: 10 February 2022

Accepted: 21 March 2022

Published: 24 March 2022

Publisher's Note: MDPI stays neutral with regard to jurisdictional claims in published maps and institutional affiliations.



Copyright: © 2022 by the authors. Licensee MDPI, Basel, Switzerland. This article is an open access article distributed under the terms and conditions of the Creative Commons Attribution (CC BY) license (<https://creativecommons.org/licenses/by/4.0/>).

Abstract: The sub-continental mantle beneath North China Craton (NCC) has attracted extensive attention in the past decades because of its dramatic transformation from an old, cold, thick, and refractory mantle to a juvenile, hot, thinner, and fertile mantle. However, the transformation mechanism remains largely controversial. The mantle xenoliths entrapped in basalts, as petrogenetic indicators, can provide an important window to reveal the evolution of the sub-continental lithospheric mantle. In this study, we present a systematical study on the geochemical characteristics of the olivine websterite xenoliths and their minerals in the Cenozoic basalts in the Hannuoba region located at the central orogenic belt of the NCC. The results, compared with the geochemical data of Paleozoic and Mesozoic peridotites, the Cenozoic composite pyroxenites as well as the global cumulate pyroxenites, demonstrate that: (1) The source of the websterite is probably the lithospheric mantle, which is mainly newly accreted, but with small amounts of ancient mantle residues. The source may be contaminated by different degrees of crustal materials. The high Nb/Ta ratios (11.36–20.57) of the websterite indicate that the Ti-bearing minerals (such as rutile) are probably involved in the source; (2) The websterite is more likely to be produced as a result of interaction of mantle peridotite with the silica-rich melts that are mainly derived from the asthenospheric mantle and also contributed by the crustal materials; (3) The metasomatic crustal melts might be derived from the subducted Paleo-Pacific plate. These melts interacted with the lithospheric mantle can significantly transform the chemical composition of the lithospheric mantle, and consequently play an important role in the destruction of the NCC. An important implication for the destruction of the NCC is further discussed.

Keywords: North China Craton (NCC); Hannuoba region; websterite xenoliths; Cenozoic basalts; peridotite-melt interaction; subducted Paleo-Pacific plate; destruction of NCC

1. Introduction

Craton is a relatively stable structural unit on the Earth's surface, consisting of the continental crust and lower sub-continental lithospheric mantle. The sub-continental lithospheric mantle, which is an important link between the asthenospheric mantle and the crust, can not only provide important information on the crust–mantle interaction and lithosphere–asthenosphere mantle interaction, but determine the basic modes of various geological processes on the continent. Generally, the sub-continental lithospheric mantle beneath the craton (e.g., Kaapvaal and Siberian Cratons) is characterized by refractory, low geothermal gradient, old age, low density, thick lithospheric root, stable structure, and

lack of large-scale volcanic-tectonic activities [1–3]. However, these characteristics are not applicable to the North China Craton (NCC).

The petrological, mineralogical, and geochemical studies on the mantle xenoliths in the Paleozoic kimberlites from both sides of the Tanlu fault zone (e.g., Mengyin, Fuxian) and in the Mesozoic gabbro and pyroxene diorite from the west side of the Tanlu fault zone (e.g., western Shandong), as well as the Cenozoic basalts and their xenoliths in the central orogenic belt (e.g., Hannuoba, Hebi, Junan, and Jiaodong) in the NCC indicate that the NCC has undergone large-scale thinning, and also a dramatic transformation (also known as “destruction”) of the lithospheric mantle from an old, cold, thick, and refractory mantle to a juvenile, hot, thinner, and fertile mantle [4–16]. Due to these unique characteristics, the NCC has attracted extensive interest in the past decades, and its thinning mechanism has been hotly debated. Various models have been proposed for elucidating the thinning mechanism from different angles, which are shown as follows:

(1) Delamination of lithospheric mantle or lower crust [17–19]. This model assumes that the thinning of the lithosphere is ultimately caused by the delamination of the lower crust or lithospheric mantle due to the metamorphism of mafic rocks into eclogites, which thickens the lower crust and increases the density of the lower crust.

(2) Thermal chemical erosion [7,8]. This model considers that the upwelling of hot materials from the asthenosphere into the lithosphere subsequently causes the melting of the lithosphere and melt removal, and consequently results in the thinning of the lithosphere mantle.

(3) Mantle replacement [15]. This model proposes that the newly accreted mantle materials, which erode and transform the ancient lithosphere, followed by the replacement of the Archean cratonic lithosphere with the Phanerozoic lithosphere, and may eventually cause the removal of the Archean lithospheric block.

(4) Water softening lithospheric mantle [20]. This model supposes that the fluids (e.g., H₂O) released by subducted plates infiltrate into the lithospheric mantle, and transform the lithospheric mantle into asthenosphere mantle, consequently leading to the lithosphere thinning.

(5) Peridotite-melt interaction [10]. This model suggests that the melts which penetrate into the lithospheric mantle and interact with the mantle peridotite result in a dramatic transformation of the physico-chemical properties of the lithosphere.

These models reasonably explain some geological processes to varying degrees. However, they were not universally accepted for lack of sufficient evidences. Therefore, new evidences are needed.

The deep mantle xenoliths entrapped by the basalts (e.g., pyroxenite and peridotite), as petrogenetic indicators, can provide an important window to explore the formation and evolution of the sub-continental lithosphere as they record the physico-chemical properties of the lithospheric mantle and also spatially and temporally reveal various deep geological processes in the lithosphere (e.g., crust–mantle interaction and lithosphere–asthenosphere interaction). The mantle xenoliths (e.g., pyroxenite, peridotite) entrapped in the Cenozoic basalts are widely distributed in eastern China. In this study, we systematically study the geochemical characteristics of the olivine (Ol) websterite xenoliths and the minerals entrapped in the Cenozoic basalts from Hannuoba to elucidate the origin of the websterite and the nature of the mantle source and reveal the source and nature of the metasomatic melts, and to further provide important constraints on the transformation of the lithospheric mantle beneath the NCC. The implication for the destruction of the NCC is further discussed.

2. Geological Setting

The North China Craton, also known as the North China block, is one of the main ancient cratons in China (Figure 1a). It can be divided into three main parts: the western block, the central orogenic belt, and the eastern block, according to the distinctions of age, tectonic evolution, lithologic association, and p-T-t path of the metamorphic basement [21–23] (Figure 1b).

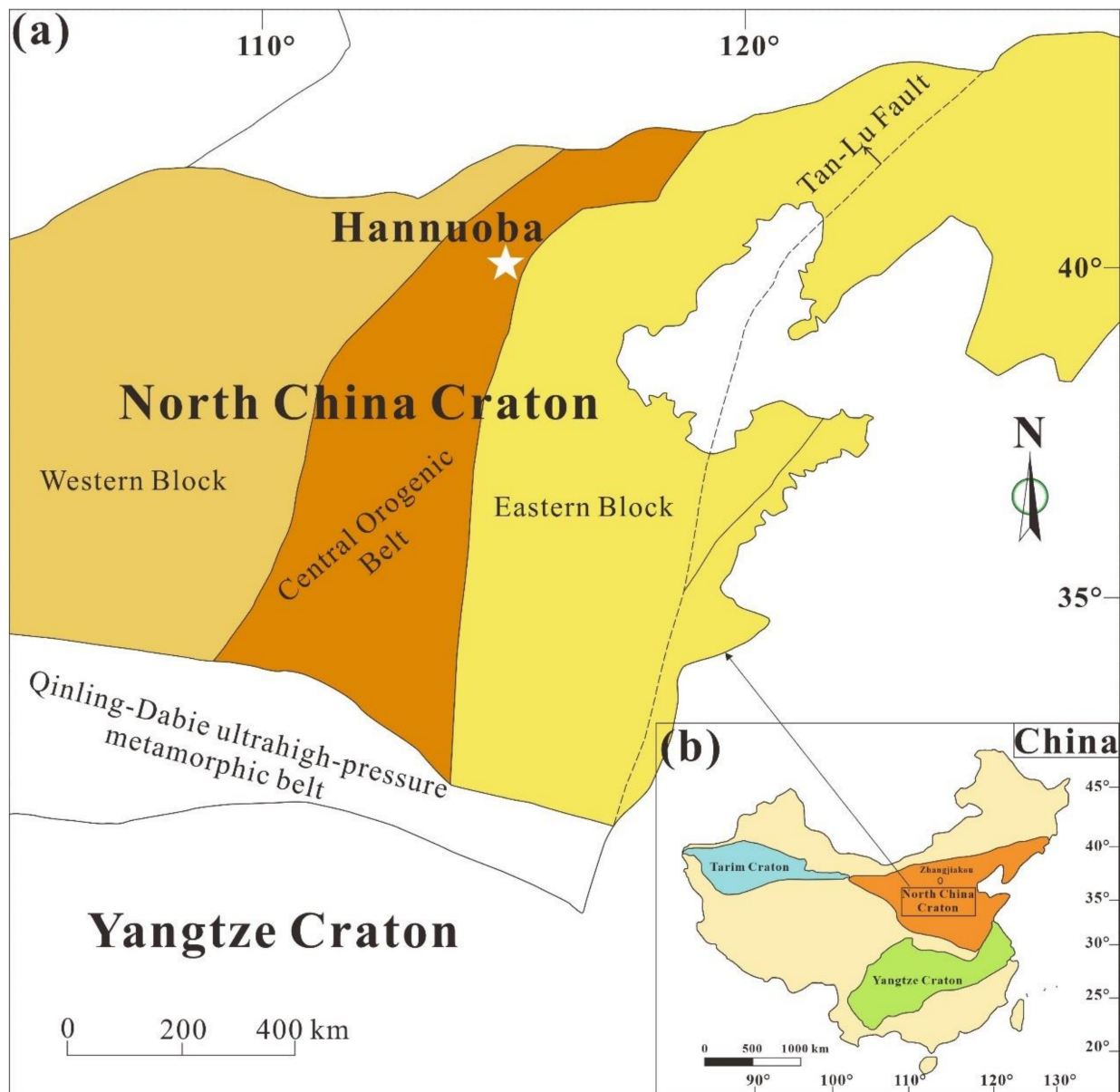


Figure 1. (a) Geographical map showing the distribution of the cratons in China (modified after Zhou et al. [24]); (b) Tectonic subdivisions of North China Craton and the geographic location of Hannuoba. Note: White star represents Hannuoba Region (modified after Gao et al. [17]).

From the time of cratonization (~1.8 Ga) up to Paleozoic, the North China Craton remained cold and relatively stable, with a thick (>200 km) Archean lithospheric root preserved. The deep xenoliths in kimberlites are rich in peridotites, with some occurrence of phlogopites and pyroxenites [24]. These peridotites are mainly refractory harzburgites, which are widely distributed in Mengyin, Shandong Province, and Fuxian, Liaoning Province [5]. The $Mg^\#$ ($Mg^\# = 100 Mg^{2+} / (Mg^{2+} + Fe^{2+})$) of olivines in these rocks are generally > 92 [25], and the lithospheric mantle is depleted in basaltic components (e.g., Al_2O_3 and CaO), indicating highly refractory residue after melt extraction [25].

However, extensive magmatism and tectonism has occurred since the Mesozoic, producing a large amount of mineral resources [26]. The lithospheric mantle in Cenozoic became hot and thin, indicating a typical “oceanic” mantle [4,5]. The xenolith types which are dominated by lherzolites in the Cenozoic basalts are simpler than those in Paleozoic kimberlites [4]. The $Mg^\#$ of olivines in these rocks are <90, much lower than those in the Paleozoic mantle peridotite. In addition, basaltic components such as Al_2O_3 and CaO are

relatively enriched in the Cenozoic lithospheric mantle [25]. These studies suggest that the lithospheric mantle of the North China Craton has transformed from cold, thick, and refractory in Paleozoic to hot, thin, and fertile in Cenozoic.

Hannuoba is located in the central orogenic belt of the NCC, adjacent to the western block of North China (Figure 1b). Abundant Cenozoic (i.e., late Tertiary) basaltic rocks are distributed in the Hannuoba. These rocks are mainly alkaline basalt and tholeiite as well as transitional types. The crustal xenoliths in basalts are felsic and mafic granulites, and the mantle xenoliths mainly include lherzolite (mainly spinel lherzolite), and pyroxenite (mainly garnet and spinel-bearing pyroxenite) [8,27–32].

Pyroxenite, one usual rock type in mantle, is considered an important part of the sources of Oceanic Island Basalts (OIBs) [33,34], Mid-Oceanic Ridge Basalts (MORBs) [35], and Island Arc Basalts (IABs) [36], providing an important window to understand the magma source of basaltic melts, the formation of continental crust, and the composition and heterogeneity of mantle. In this sense, we choose the pyroxenites in the Cenozoic basalts from Hannuoba as the object of this study.

The sampling location is located in Jieshaba, Zhangjiakou city, Hebei Province (Figures 1 and 2) and the samples chosen in this study are olivine (Ol) websterite, with the mineral assemblage of Ol + Opx + Cpx + Sp ± Grt. The major minerals are orthopyroxene (Opx) and clinopyroxene (Cpx) (Figure 3a–f), and the minor minerals are olivine (Ol) (Figure 3e,f). The accessory minerals are spinel (Sp) and (or) garnet (Grt). Olivines are typically olive green in hand specimens, while clinopyroxene is emerald green, and orthopyroxene is brown, with a small amount of opaque spinel. Most of the samples show residual porphyritic. Olivine displays plate or granular crystalloblastic, which are elongated in various degrees, with developed kinks; some parts between olivine and pyroxene particles show contact of triple points with balanced structure, with a straight boundary (Figure 3e,f). There are small amounts of spinel, which are randomly distributed in the gap between pyroxene particles (Figure 3e,f).

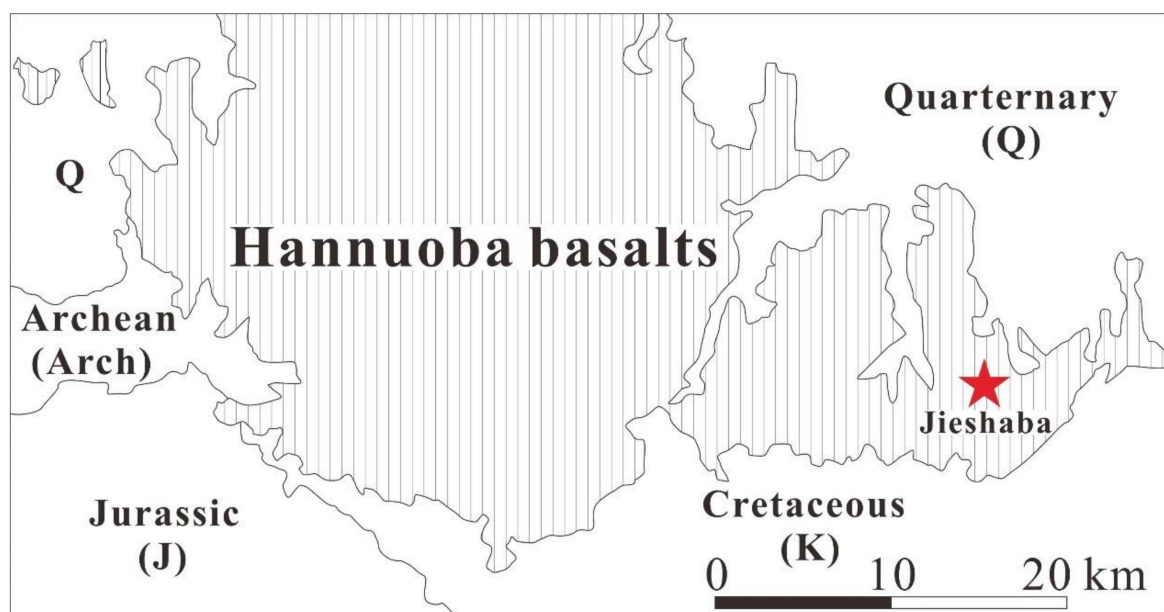


Figure 2. Sampling location of the websterite studied. Note: The red star indicates the sampling location. Stratigraphic abbreviations: Arch—Archean terrain, J—Jurassic, K—Cretaceous, Q—Quarternary (modified after Zhou et al. [24]).

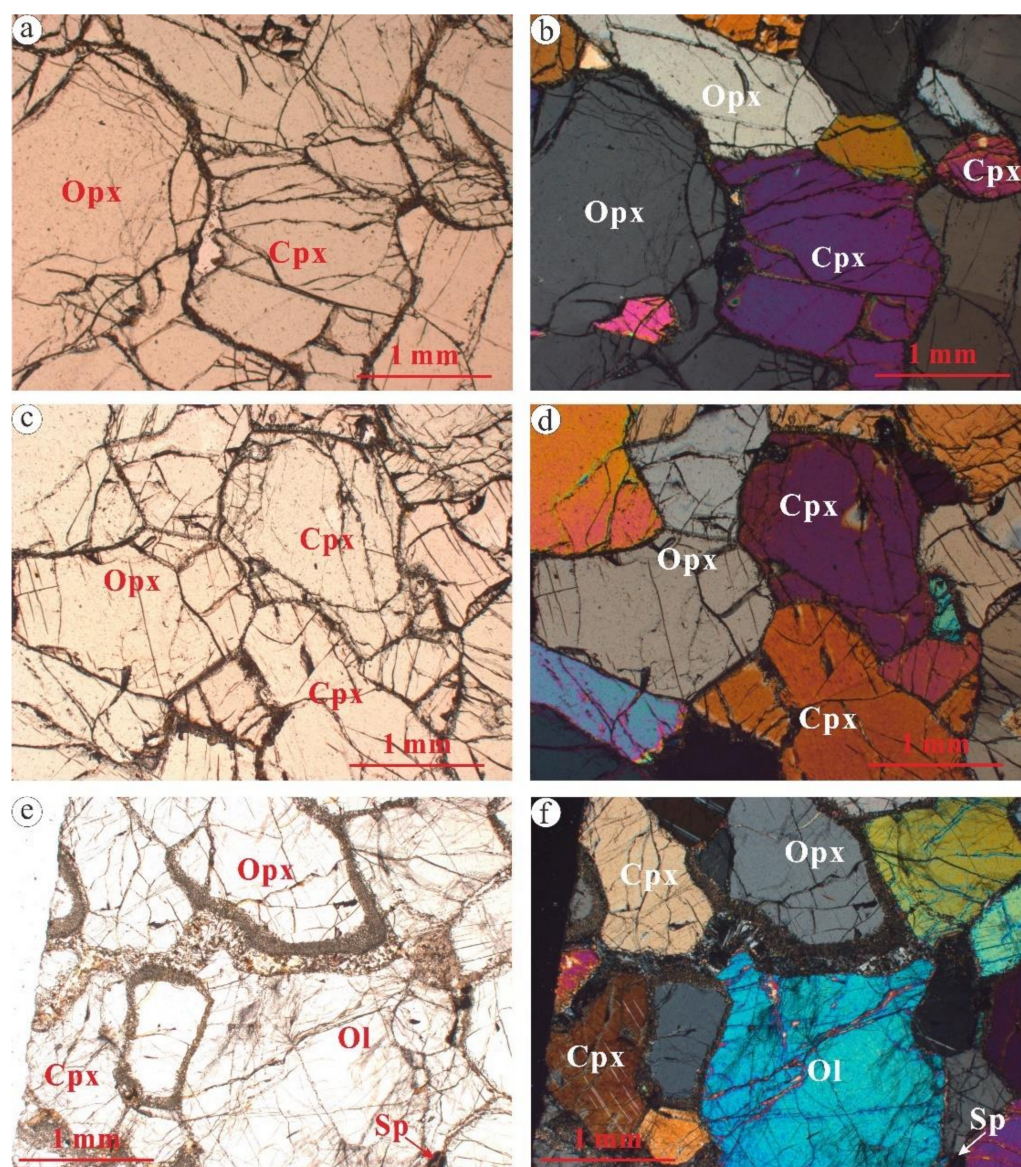


Figure 3. Photomicrographs of the websterite xenoliths from Hannuoba, with the plane-polarized (a,c,e) and cross-polarized light (b,d,f), respectively, showing the mineral assemblage of olivine + orthopyroxene + clinopyroxene + Sp. Abbreviations: Cpx: clinopyroxenite; Opx: orthopyroxene; Ol: olivine; Sp: Spinel.

3. Analytical Methods

The chemical compositions of minerals were determined by electron probe microanalyses (EMPA) using the JEOL JXA-8100 electron microprobe (Jeol Ltd., Tokyo, Japan). The accelerating voltage and current were 15 KV and 12 nA, respectively. The beam diameter was 5 μm , and the counting time was 10–30 s. The standard minerals (e.g., pyroxene, albite, Cr_2O_3 , and Fe_2O_3) were used for calibration. The analytical accuracy is better than $\pm 2\%$ for major elements.

The major elements of the whole rock were analyzed by X-ray fluorescence spectrometry (XRF) after the mixture of whole rock powder (0.5 g) and $\text{Li}_2\text{B}_4\text{O}_7 + \text{LiBO}_2$ (5 g) in the glass disk. For the analysis of trace elements, the whole rock powder (40 mg) was added to a Teflon bottle, dropped into $\text{HF} + \text{HNO}_3$, and then placed in a steel tank in the incubator at 200 $^\circ\text{C}$ for 5 days. The heated Teflon bottle was taken out and evaporated to dryness on the heating pot, and then digested with HNO_3 at 150 $^\circ\text{C}$ for one day. The final step was repeated. The dissolved sample was diluted with 49 mL 1% HNO_3 and 1 mL

500 ppb standard solution. Finally, the trace elements were determined by ICP-MS. The analytical accuracies of major and trace elements are within $\pm 2\%$ and $\pm 5\%$, respectively. The elements, such as Si, Ti, Al, Fe, Mn, Mg, Ca, Na, K, P, Fe^{2+} , Fe^{3+} , Rb, Ba, Th, U, Nb, Ta, La, Ce, Pb, Pr, Sr, Nd, Zr, Hf, Sm, Eu, Ti, Gd, Dy, Li, Ho, Er, Y, Yb, Lu, Cr, Tb, and Tm were determined.

All the analyses mentioned above were completed at the Institute of Geology and Geophysics, Chinese Academy of Sciences (IGGCAS).

4. Results

4.1. Major and Trace Elements of the Whole Rocks

4.1.1. Major Elements

The major elements of the websterites from Hannuoba are presented in Table 1. The SiO_2 contents of the Ol websterite are 45.7–51.0 wt%, falling in the field of mafic rocks. The contents of MgO, Al_2O_3 , CaO, Na_2O , K_2O , and TiO_2 are 17.3–32.2 wt%, 3.69–12.40 wt%, 5.06–13.00 wt%, 0.44–1.61 wt%, 0.03–0.47 wt%, and 0.25–0.70 wt%, respectively. The $\text{Mg}^\#$ of the websterite are relatively low ($\text{Mg}^\# = 83.4\text{--}90.1$).

Figure 4 shows that there is a good negative correlation between $\text{Mg}^\#$ and Al_2O_3 , TiO_2 , MnO, Na_2O , and K_2O . Except for small amounts falling in the field of Mesozoic peridotite (Figure 4c,e,h), most of the data studied fall into the field of Cenozoic composite pyroxenite. Some scattered data fall into the fields of the Hannuoba Cr-pyroxenite (Figure 4a,e,g,h) and the global cumulate pyroxenite (Figure 4f,h).

4.1.2. Trace Elements of the Whole Rock

The trace elements of the websterites from Hannuoba are presented in Table 1. In the primitive mantle-normalized trace element patterns of the websterite (Figure 5), most samples resemble the oceanic island basalt (OIB), indicating that the websterite might originate from the mantle source metasomatized by the asthenosphere melts. Some samples are rich in LILE (e.g., Rb, Ba, U, Pb, Sr) and relatively depleted in HFSE (e.g., Nb, Ta, Zr, Hf), suggesting that crustal materials may be involved in the source of the websterite. It is worth noting that some samples are depleted in Th, implying that the samples may be inherited from the geochemical characteristics of the depleted mantle. In addition, it can be also found that the trace element distribution patterns of most samples studied are similar to those of Cenozoic composite pyroxenites, but significantly distinct from those of Paleozoic garnet pyroxenite and Mesozoic wehrlites (Figure 5).

REE, LREE, and HREE of the websterites from Hannuoba are largely variable ($\sum \text{REE} = 9.66\text{--}67.28$ ppm, $\sum \text{LREE} = 5.10\text{--}57.28$ ppm, $\sum \text{HREE} = 2.37\text{--}16.79$ ppm, Table 1), suggesting that the source of the websterite may be affected by different degrees of contamination from crustal materials. $(\text{La}/\text{Yb})_N$ and $(\text{Dy}/\text{Yb})_N$ are 0.44–2.88 and 0.73–1.74, respectively, indicating insignificant HREE fractionation, whereas $\text{LREE}/\text{HREE} = 1.00\text{--}5.73$, implying LREE enrichment in some samples. The chondrite-normalized REE patterns of the Hannuoba websterite xenoliths (Figure 6) show that LREE are either enriched or slightly depleted in some samples. The Eu is weakly depleted in the websterite on the whole and does not show an upward inverted “U” type distribution pattern, suggesting the websterite is not cumulate origin. However, the distinction of REE distribution patterns may reflect the heterogeneity of the mantle source of the websterite, as can be seen from the comparison between the REE distribution patterns of websterite and other mantle-derived rocks (i.e., N-MORB, E-MORB and OIB) (Figure 6).

Table 1. Major (wt%) and trace element (ppm) compositions of the websterite xenoliths.

Sample	JSB10-43	JSB10-47	JSB10-02	JSB10-19	JSB10-24	JSB10-31	JSB10-27	JSB10-13	JSB10-16	JSB10-06	JSB10-11
SiO ₂	51.00	50.50	45.70	46.60	47.60	46.10	47.00	46.70	50.60	48.80	48.90
TiO ₂	0.25	0.31	0.26	0.37	0.39	0.33	0.47	0.37	0.48	0.41	0.70
Al ₂ O ₃	3.69	7.26	6.42	7.54	9.40	5.84	7.73	7.49	8.19	9.86	12.40
TFe ₂ O ₃	6.29	6.13	8.42	8.16	7.31	9.17	9.21	9.23	5.59	7.09	6.89
MnO	0.11	0.13	0.14	0.12	0.14	0.13	0.14	0.14	0.13	0.17	0.17
MgO	28.50	23.10	32.20	28.10	24.90	31.50	28.20	28.50	18.70	22.10	17.30
CaO	8.86	10.60	5.06	6.53	7.97	5.38	5.31	5.69	13.00	8.73	10.70
Na ₂ O	0.44	0.88	0.67	1.26	0.88	0.48	0.90	0.77	1.41	1.03	1.61
K ₂ O	0.03	0.03	0.23	0.24	0.15	0.07	0.42	0.23	0.42	0.34	0.47
P ₂ O ₅	0.01	0.02	0.03	0.05	0.04	0.03	0.08	0.04	0.10	0.04	0.11
LOI	0.30	0.48	0.48	0.66	0.94	0.58	0.50	0.84	0.80	1.38	1.06
FeO	4.30	4.02	6.46	6.03	4.98	6.60	7.05	6.68	3.80	5.34	4.95
Fe ₂ O ₃	1.51	1.67	1.25	1.46	1.78	1.83	1.38	1.80	1.37	1.16	1.39
Mg [#]	90.10	88.30	88.40	87.30	87.20	87.30	86.00	86.00	87.00	86.20	83.40
CaO/Al ₂ O ₃	2.40	1.46	0.79	0.87	0.85	0.92	0.69	0.76	1.59	0.89	0.86
Li	1.77	1.64	1.98	2.67	2.61	2.39	3.61	3.27	4.44	1.52	3.88
Be	0.08	0.15	0.06	0.20	0.10	0.04	0.23	0.14	0.42	0.10	0.30
Sc	21.20	36.70	23.90	22.90	34.90	22.00	23.40	26.90	47.10	45.50	42.50
V	127.00	161.00	112.00	128.00	152.00	136.00	137.00	131.00	237.00	220.00	298.00
Cr	6676.00	5291.00	2422.00	2116.00	2783.00	2717.00	2351.00	2374.00	2744.00	1435.00	978.00
Co	62.20	53.80	80.20	74.60	63.90	85.20	78.30	75.80	42.50	45.30	41.80
Ni	1135.00	951.00	1623.00	1192.00	1309.00	1698.00	1315.00	1250.00	725.00	654.00	626.00
Cu	38.30	83.30	37.30	44.50	133.00	58.90	34.90	32.80	136.00	29.80	87.50
Zn	38.80	38.80	50.70	47.80	44.90	61.60	63.20	57.10	28.60	26.40	28.40
Ga	4.63	7.13	5.57	7.18	7.57	5.86	8.41	6.52	7.69	8.58	12.24
Rb	0.69	1.17	4.38	4.25	4.25	2.22	6.31	4.70	8.81	8.40	6.93
Sr	37.30	52.90	113.00	82.30	67.40	44.60	143.00	154.00	278.00	175.00	177.00
Y	2.78	8.86	7.79	7.49	11.70	6.38	10.10	9.22	14.20	18.70	25.90
Zr	7.94	17.00	16.20	30.00	27.80	16.50	35.70	23.70	39.00	30.10	50.80
Nb	0.98	1.59	1.44	4.14	1.82	0.75	5.43	3.04	8.96	2.64	7.98
Cs	0.02	0.04	0.03	0.01	0.02	0.02	0.03	0.02	0.04	0.01	0.02
Ba	10.60	9.76	31.20	38.70	22.90	16.20	87.60	28.00	66.50	48.40	74.10

Table 1. Cont.

Sample	JSB10-43	JSB10-47	JSB10-02	JSB10-19	JSB10-24	JSB10-31	JSB10-27	JSB10-13	JSB10-16	JSB10-06	JSB10-11
La	1.06	2.11	0.69	2.47	1.11	0.40	3.56	1.67	11.00	1.55	5.38
Ce	2.73	4.61	1.86	5.58	3.47	1.43	7.38	4.15	24.80	4.10	10.50
Pr	0.48	0.70	0.32	0.79	0.56	0.31	1.02	0.59	3.54	0.62	1.45
Nd	2.47	3.48	1.78	3.72	3.00	1.94	4.61	2.91	14.30	3.08	6.82
Sm	0.73	1.09	0.60	1.09	1.02	0.73	1.29	0.92	2.82	1.09	2.10
Eu	0.24	0.38	0.25	0.37	0.39	0.28	0.41	0.31	0.84	0.40	0.80
Gd	0.74	1.27	0.90	1.29	1.45	1.00	1.53	1.20	2.72	1.55	3.00
Tb	0.12	0.24	0.18	0.23	0.29	0.19	0.30	0.24	0.45	0.37	0.64
Dy	0.70	1.69	1.35	1.50	2.15	1.30	2.00	1.69	2.64	2.75	4.47
Ho	0.13	0.37	0.31	0.30	0.49	0.29	0.44	0.38	0.58	0.71	1.05
Er	0.33	1.06	0.88	0.87	1.42	0.81	1.25	1.09	1.58	2.18	3.11
Tm	0.04	0.16	0.14	0.13	0.22	0.12	0.19	0.17	0.24	0.37	0.51
Yb	0.26	1.09	0.90	0.85	1.52	0.75	1.22	1.14	1.57	2.54	3.47
Lu	0.04	0.18	0.14	0.13	0.24	0.11	0.19	0.18	0.23	0.41	0.53
Hf	0.27	0.51	0.43	0.83	0.74	0.52	0.93	0.64	0.97	0.71	1.41
Ta	0.06	0.14	0.07	0.24	0.11	0.04	0.33	0.17	0.72	0.16	0.51
Tl	0.00	0.01	0.01	0.02	0.02	0.01	0.02	0.01	0.02	0.01	0.01
Pb	0.30	0.46	0.72	0.15	0.16	0.07	0.68	0.27	0.67	0.30	0.47
Bi	0.00	0.01	0.01	0.00	0.00	0.00	0.00	0.00	0.01	0.00	0.00
Th	0.09	0.15	0.08	0.32	0.11	0.02	0.50	0.21	1.13	0.18	0.69
U	0.03	0.09	0.03	0.11	0.08	0.02	0.23	0.07	0.28	0.06	0.19
Nb/Ta	16.33	11.36	20.57	17.25	16.55	18.75	16.45	17.88	12.44	16.50	15.65
Zr/Hf	29.41	33.33	37.67	36.14	37.57	31.73	38.39	37.03	40.21	42.39	36.03
∑ REE	10.07	18.42	10.28	19.31	17.32	9.66	25.39	16.63	67.28	21.70	43.83
LREE	7.70	12.36	5.49	14.00	9.54	5.10	18.27	10.55	57.28	10.84	27.04
HREE	2.37	6.06	4.79	5.31	7.77	4.56	7.12	6.08	10.00	10.86	16.79
LREE/HREE	3.25	2.04	1.14	2.64	1.23	1.12	2.57	1.74	5.73	1.00	1.61
(La/Yb) _N	2.85	1.39	0.55	2.08	0.52	0.38	2.10	1.06	5.06	0.44	1.11
δEu	0.99	0.98	1.02	0.95	0.97	1.01	0.90	0.90	0.92	0.93	0.98

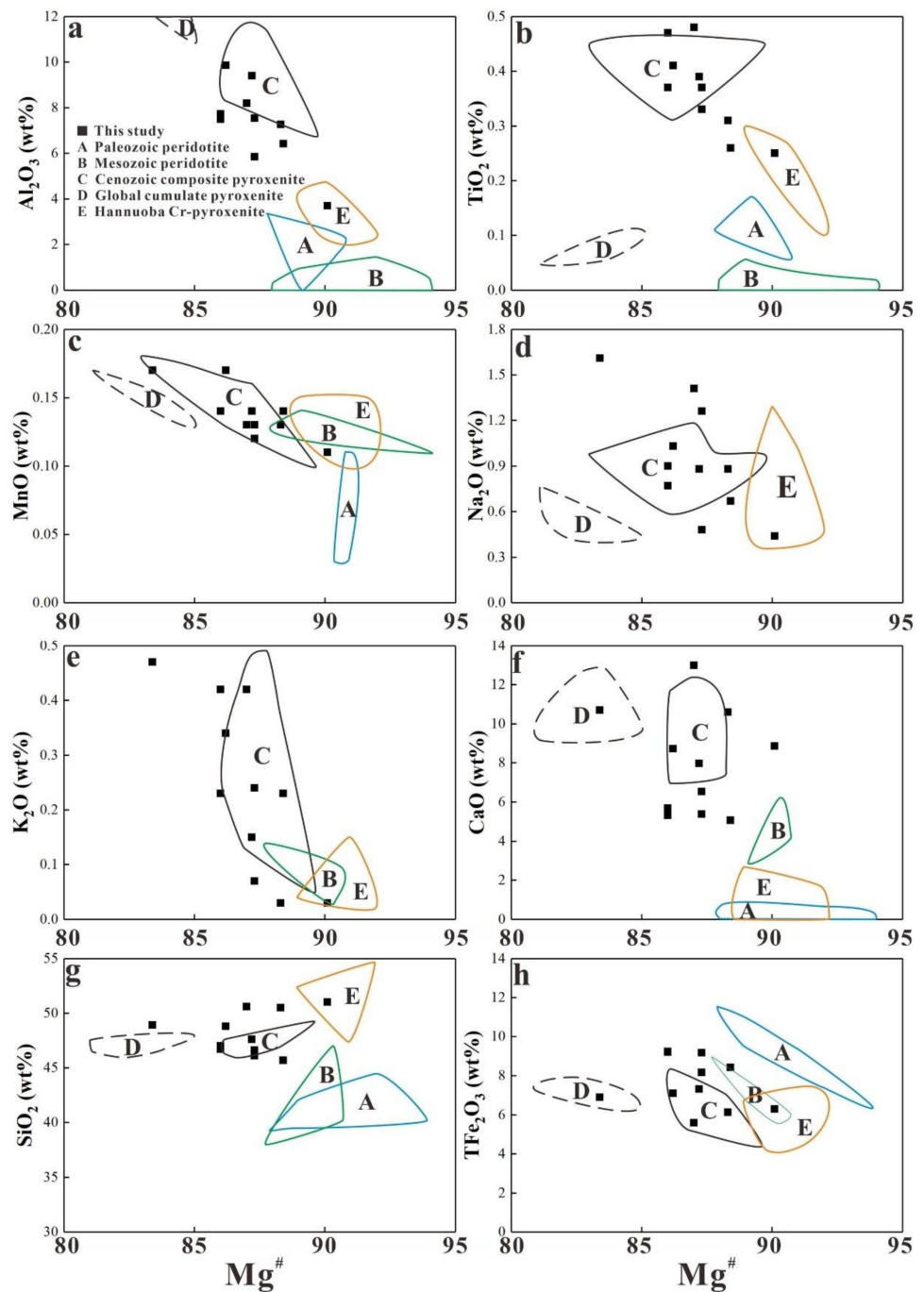


Figure 4. Harker diagrams for major element compositions of the websterite xenoliths from Hannuoba. (a): Plots of $Mg^{\#}$ vs. Al_2O_3 ; (b): Plots of $Mg^{\#}$ vs. TiO_2 ; (c): Plots of $Mg^{\#}$ vs. MnO ; (d): Plots of $Mg^{\#}$ vs. Na_2O ; (e): Plots of $Mg^{\#}$ vs. K_2O ; (f): Plots of $Mg^{\#}$ vs. CaO ; (g): Plots of $Mg^{\#}$ vs. SiO_2 ; (h): Plots of $Mg^{\#}$ vs. TFe_2O_3 . Note: the Paleozoic peridotite represents the remnant of Archean lithospheric mantle after partial melting [37]; the Mesozoic peridotite represents the residual Archean lithospheric mantle, which was later transformed by the mantle metasomatism involving the continental crust materials [37]; Cenozoic composite pyroxenites represents the product of peridotite-melt interaction [38]; the global cumulate pyroxenite represents pyroxenite with the cumulate origin [39]; Cr-pyroxenite of Hannuoba represents the residual residual-genetic pyroxenite through different degrees of melting of the primitive mantle [40].

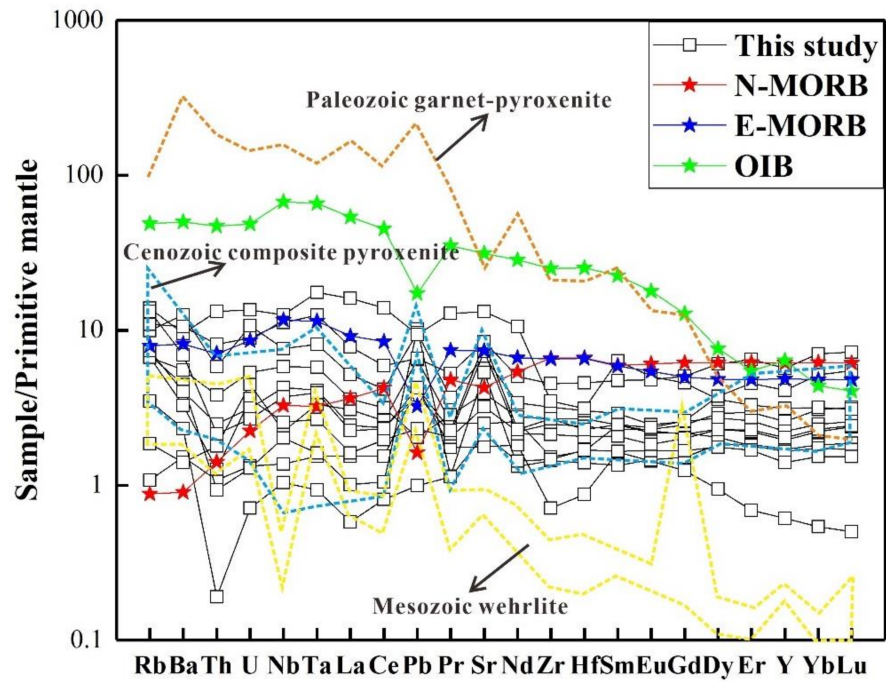


Figure 5. Primitive mantle-normalized trace element patterns of the Hannuoba websterite xenoliths. Note: Paleozoic garnet pyroxenite represents the pyroxenite with the origin of melt crystallization [41]; Mesozoic wehrlite represents the pyroxenite formed by the interaction between peridotite and the melt from recycled continental crust materials [42]; Cenozoic composite pyroxenite represents the pyroxenite by peridotite-melt interaction [38]; Data of primitive mantle, normal mid ocean ridge basalt (N-MORB), enriched mid ocean ridge basalt (E-MORB) and ocean island basalt (OIB) are sourced from Sun and McDonough [43].

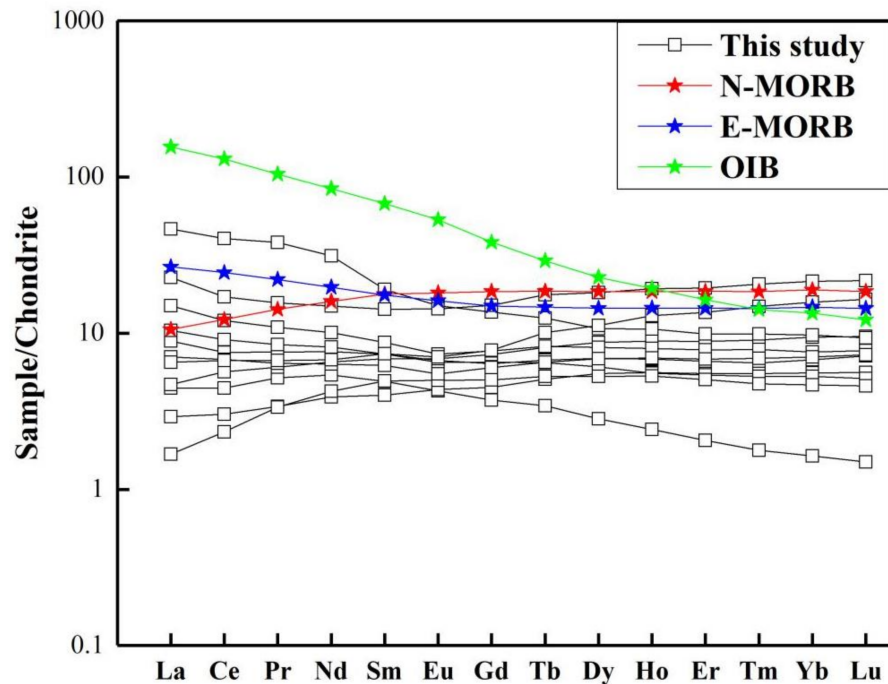


Figure 6. Chondrite-normalized REE patterns of the Hannuoba websterite xenoliths. Note: The data for the primitive mantle, N-MORB, E-MORB, and OIB are the same as Figure 5.

4.2. Mineral Compositions

The major element compositions of the minerals (i.e., Ol, Cpx, Opx, Sp) are shown in Tables 2–5 and Figures 7–12, compared with those of the peridotites from Hebi [15] that represent the residual old mantle, and the peridotites from Shanwang [41] that represent the juvenile mantle (Figure 7).

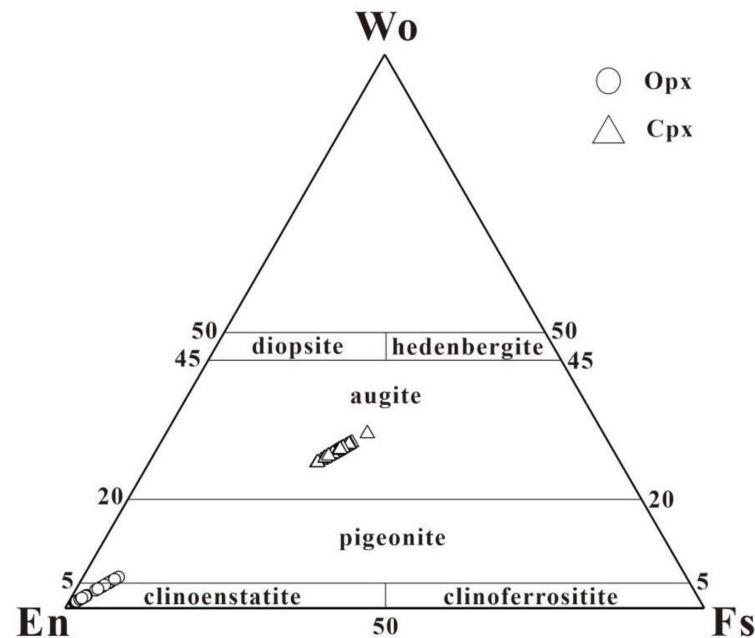


Figure 7. Wo-En-Fs diagram of the orthopyroxene (Opx) and clinopyroxene (Cpx) in the websterite (modified after Morimoto [44]).

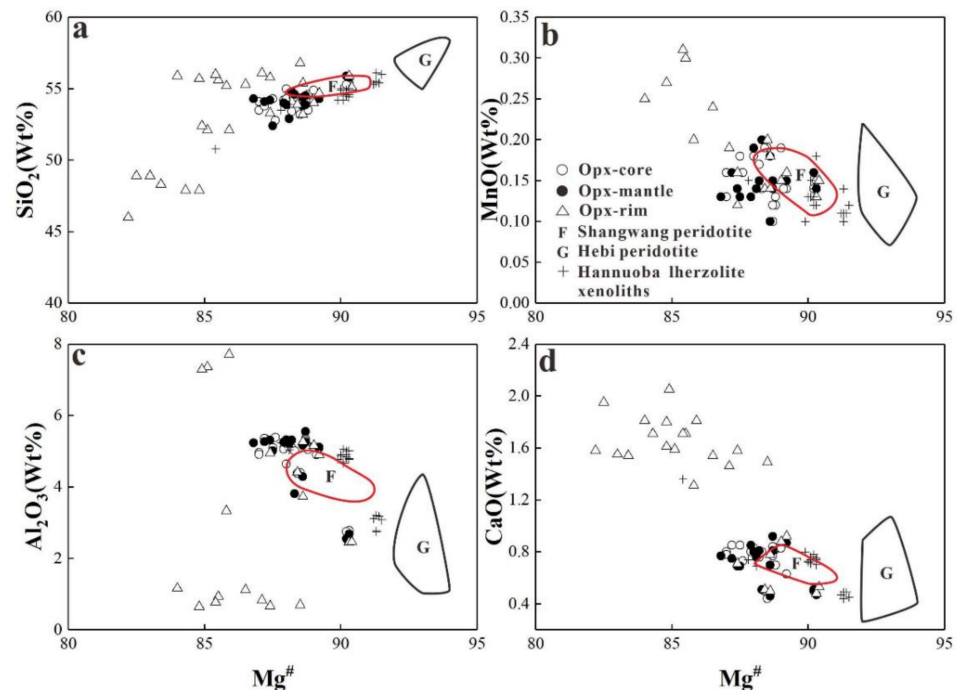


Figure 8. Plots of $Mg^{\#}$ vs. SiO_2 (a), MnO (b), Al_2O_3 (c) and CaO (d) for the orthopyroxene (Opx) in the websterite. Note: The Shanwang peridotite is characterized by a fertile mantle, which represents the newly-accreted lithospheric mantle [41]; the Hebi peridotite represents the remnant of the old cratonic lithospheric mantle [15].

Table 2. The major element composition of orthopyroxene (Opx) in the websterite determined by EMPA.

Sample	Position-Particle	SiO ₂	TiO ₂	Al ₂ O ₃	Cr ₂ O ₃	FeO	MnO	MgO	CaO	Na ₂ O	K ₂ O	NiO	Mg [#]	Fs	Wo	En
JSB10-43	core-1	55.40	0.11	2.78	0.44	6.45	0.15	33.30	0.47	0.01	0.00	0.10	90.30	9.60	0.90	89.50
	mantle-1	55.80	0.16	2.68	0.45	6.45	0.14	33.40	0.47	0.08	0.01	0.07	90.30	9.60	0.90	89.50
	rim-1	55.90	0.14	2.45	0.42	6.51	0.13	33.60	0.48	0.03	0.00	0.03	90.30	9.60	0.92	89.40
	core-2	55.30	0.15	2.75	0.38	6.55	0.14	33.50	0.50	0.08	0.00	0.11	90.20	9.70	0.96	89.30
	mantle-2	55.90	0.15	2.55	0.35	6.47	0.16	33.00	0.51	0.03	0.01	0.07	90.20	9.70	0.99	89.30
	rim-2	55.10	0.13	2.46	0.37	6.32	0.15	33.10	0.53	0.00	0.00	0.09	90.40	9.50	1.02	89.50
JSB10-47	core-1	53.20	0.11	4.40	0.26	7.42	0.19	31.60	0.44	0.10	0.00	0.06	88.50	11.40	0.87	87.70
	mantle-1	53.80	0.10	4.29	0.36	7.39	0.18	31.80	0.46	0.05	0.00	0.14	88.60	11.30	0.90	87.80
	rim-1	53.90	0.11	4.41	0.33	7.46	0.14	31.70	0.51	0.06	0.02	0.07	88.40	11.40	1.00	87.60
	core-2	54.40	0.12	4.38	0.32	7.47	0.19	31.60	0.50	0.03	0.01	0.08	88.40	11.50	0.98	87.50
	mantle-2	54.60	0.05	3.81	0.22	7.44	0.20	31.20	0.51	0.15	0.04	0.07	88.30	11.60	1.01	87.40
	rim-2	55.40	0.11	3.73	0.15	7.54	0.14	32.50	0.50	0.06	0.01	0.13	88.60	11.30	0.96	87.70
JSB10-02	core-1	54.50	0.17	5.14	0.22	6.95	0.12	30.70	0.82	0.20	0.00	0.09	88.80	11.00	1.66	87.40
	rim-1	56.80	0.69	0.70	0.36	7.48	0.20	31.90	1.49	0.07	0.00	0.05	88.50	11.20	2.87	86.00
	core-2	54.50	0.24	5.11	0.20	6.86	0.14	31.40	0.63	0.18	0.00	0.10	89.20	10.70	1.27	88.00
	mantle-2	54.30	0.25	5.09	0.17	6.84	0.15	31.30	0.87	0.12	0.01	0.13	89.20	10.60	1.75	87.60
JSB10-19	core-1	53.50	0.15	5.11	0.26	7.03	0.13	30.90	0.83	0.13	0.00	0.13	88.80	11.00	1.66	87.30
	rim-1	53.20	0.14	5.26	0.30	7.03	0.18	30.40	0.78	0.25	0.00	0.10	88.60	11.20	1.61	87.20
	core-2	54.10	0.17	5.35	0.30	7.04	0.12	30.80	0.84	0.13	0.00	0.11	88.70	11.10	1.70	87.20
	mantle-2	54.50	0.12	5.25	0.28	7.06	0.15	30.80	0.92	0.17	0.01	0.06	88.70	11.10	1.85	87.10
	rim-2	55.80	0.74	0.67	0.20	8.13	0.16	31.40	1.58	0.07	0.01	0.04	87.40	12.20	3.04	84.80
	core-3	54.60	0.24	5.04	0.19	7.01	0.13	30.80	0.70	0.17	0.01	0.11	88.80	11.10	1.42	87.50
JSB10-16	core-2	54.90	0.12	5.12	0.24	7.03	0.19	31.50	0.83	0.11	0.00	0.11	89.00	10.90	1.65	87.50
	rim-2	54.00	0.16	5.16	0.26	6.92	0.15	30.90	0.88	0.14	0.00	0.07	89.00	10.80	1.78	87.40
JSB10-06	core-1	55.00	0.17	4.64	0.09	7.54	0.18	30.60	0.83	0.14	0.00	0.04	88.00	11.80	1.67	86.50
	rim-1	55.90	0.48	1.16	0.19	10.20	0.25	29.70	1.81	0.11	0.01	0.03	84.00	15.40	3.53	81.00
	core-2	54.30	0.13	5.22	0.19	7.56	0.18	30.70	0.80	0.17	0.01	0.17	88.00	11.80	1.61	86.50
	mantle-2	54.00	0.17	5.25	0.19	7.61	0.13	30.70	0.85	0.12	0.00	0.09	87.90	11.90	1.70	86.40
	rim-2	56.00	0.79	0.77	0.33	9.32	0.31	30.40	1.71	0.03	0.00	0.07	85.40	14.10	3.32	82.60

Table 2. Cont.

Sample	Position-Particle	SiO ₂	TiO ₂	Al ₂ O ₃	Cr ₂ O ₃	FeO	MnO	MgO	CaO	Na ₂ O	K ₂ O	NiO	Mg [#]	Fs	Wo	En
JSB10-11	core-1	53.80	0.17	5.36	0.14	8.08	0.16	30.40	0.85	0.16	0.01	0.07	87.20	12.60	1.71	85.70
	core-2	54.30	0.20	5.10	0.25	7.78	0.18	30.30	0.85	0.17	0.00	0.04	87.50	12.30	1.71	86.00
	mantle-2	54.20	0.22	5.31	0.22	7.91	0.14	30.40	0.69	0.18	0.00	0.10	87.40	12.50	1.40	86.10
	rim-2	56.10	0.63	0.83	0.29	8.32	0.19	31.30	1.46	0.00	0.02	0.08	87.10	12.50	2.83	84.70

Table 3. The major element composition of clinopyroxene (Cpx) in the websterite determined by EMPA.

Sample	Position-Particle	SiO ₂	TiO ₂	Al ₂ O ₃	Cr ₂ O ₃	FeO	MnO	MgO	CaO	Na ₂ O	K ₂ O	NiO	Mg [#]	Fs	Wo	En	Cr [#]
JSB10-43	core-1	52.70	0.43	4.02	1.25	2.51	0.08	15.70	21.60	1.06	0.00	0.04	91.80	4.30	47.40	48.30	17.30
	mantle-1	52.90	0.47	3.66	0.90	2.55	0.08	15.50	21.90	0.95	0.00	0.04	91.60	4.40	48.00	47.60	14.10
	rim-1	53.10	0.83	1.92	1.16	2.66	0.03	16.60	22.30	0.60	0.00	0.02	91.80	4.30	46.80	48.80	28.90
	core-2	52.80	0.37	3.93	1.05	2.55	0.11	15.60	21.20	1.06	0.00	0.03	91.70	4.40	47.10	48.50	15.10
	mantle-2	52.60	0.43	3.90	0.98	2.60	0.10	15.50	21.50	1.00	0.00	0.08	91.50	4.50	47.50	48.00	14.50
	rim-2	52.40	0.66	2.75	1.01	2.68	0.05	16.30	21.90	0.77	0.00	0.05	91.60	4.50	46.80	48.70	19.80
JSB10-47	core-1	51.20	0.56	6.16	0.62	2.84	0.07	14.60	20.70	1.52	0.03	0.08	90.30	5.10	47.70	47.20	6.30
	mantle-1	52.40	0.52	5.79	0.58	2.81	0.11	14.80	20.90	1.45	0.00	0.08	90.50	5.00	47.70	47.30	6.30
	rim-1	52.80	0.89	1.84	0.79	3.63	0.18	17.00	20.60	0.30	0.01	0.00	89.40	6.00	43.50	50.50	22.20
	core-2	51.60	0.51	6.61	0.71	2.88	0.05	14.30	20.50	1.56	0.00	0.03	90.00	5.20	47.90	46.90	6.70
	mantle-2	52.10	0.53	6.12	0.70	2.92	0.12	14.40	20.50	1.58	0.00	0.05	89.90	5.30	47.80	46.90	7.10
	rim-2	52.80	0.82	2.04	0.75	3.62	0.10	16.10	22.30	0.46	0.00	0.05	88.90	5.90	46.90	47.20	19.80
JSB10-02	core-1	51.80	0.75	7.44	0.39	3.29	0.10	14.60	18.50	2.06	0.01	0.01	88.80	6.20	44.60	49.20	3.40
	rim-1	51.70	0.74	4.38	0.54	3.21	0.05	16.50	21.60	0.47	0.00	0.06	90.20	5.30	45.80	48.90	7.60
	core-2	52.40	0.74	7.52	0.39	3.29	0.07	14.70	18.40	1.97	0.00	0.04	88.90	6.20	44.30	49.60	3.40
	rim-2	51.90	0.66	4.48	0.69	3.14	0.09	16.50	21.30	0.44	0.01	0.06	90.40	5.20	45.50	49.20	9.30

Table 3. Cont.

Sample	Position-Particle	SiO ₂	TiO ₂	Al ₂ O ₃	Cr ₂ O ₃	FeO	MnO	MgO	CaO	Na ₂ O	K ₂ O	NiO	Mg [#]	Fs	Wo	En	Cr [#]
JSB10-19	core-1	51.60	0.69	7.74	0.54	3.44	0.11	14.40	18.20	2.05	0.02	0.09	88.20	6.50	44.40	49.10	4.50
	mantle-1	51.70	0.60	7.79	0.50	3.48	0.09	14.20	18.40	2.26	0.01	0.03	88.00	6.60	44.90	48.50	4.10
	rim-1	52.10	1.71	1.75	0.68	4.68	0.16	17.30	19.60	0.45	0.02	0.04	87.00	7.70	41.30	51.00	20.60
	core-2	51.30	0.76	7.28	0.29	3.44	0.12	14.20	18.50	2.14	0.00	0.08	88.10	6.50	45.00	48.50	2.60
	mantle-2	51.40	0.72	7.53	0.32	3.51	0.04	14.40	18.40	2.16	0.00	0.07	88.00	6.60	44.70	48.70	2.80
	rim-2	51.70	0.81	3.95	0.41	4.65	0.11	15.50	21.30	0.18	0.00	0.05	85.80	7.70	45.70	46.60	6.60
	core-3	51.50	0.84	7.59	0.28	3.39	0.09	14.20	18.40	2.16	0.00	0.08	88.30	6.40	44.90	48.60	2.40
	mantle-3	52.40	0.69	7.73	0.31	3.39	0.03	14.60	18.30	2.22	0.00	0.04	88.60	6.40	44.30	49.30	2.60
rim-3	52.40	1.53	1.66	0.37	4.77	0.13	17.70	19.30	0.25	0.00	0.01	87.00	7.70	40.40	51.90	13.00	
JSB10-24	core-1	52.00	0.69	7.30	0.37	3.41	0.13	14.60	18.30	2.24	0.02	0.05	88.50	6.40	44.20	49.40	3.30
	mantle-1	51.60	0.74	7.45	0.38	3.52	0.09	14.40	18.30	2.31	0.00	0.03	88.10	6.60	44.40	49.00	3.30
	rim-1	51.10	0.93	4.02	0.47	5.13	0.10	14.90	21.30	0.48	0.00	0.03	83.90	8.70	46.20	45.20	7.20
	core-2	51.00	0.70	7.31	0.41	3.45	0.08	14.30	18.10	2.07	0.01	0.02	88.20	6.60	44.40	49.10	3.60
	mantle-2	51.40	0.67	7.46	0.41	3.34	0.12	14.40	17.50	2.30	0.01	0.05	88.60	6.50	43.60	49.90	3.50
	rim-2	50.10	1.14	3.80	0.46	4.51	0.11	15.40	21.70	0.32	0.01	0.04	86.00	7.50	46.40	46.10	7.50
	core-3	51.50	0.71	7.51	0.43	3.52	0.07	14.40	17.70	2.33	0.00	0.03	88.00	6.80	43.60	49.60	3.70
	mantle-3	51.20	0.77	7.58	0.41	3.55	0.13	14.30	18.30	2.15	0.00	0.07	87.90	6.70	44.50	48.70	3.50
rim-3	49.60	1.16	5.92	0.50	5.45	0.11	14.40	19.90	0.69	0.02	0.04	82.60	9.60	45.00	45.50	5.40	
JSB10-31	core-1	51.30	0.86	7.74	0.38	3.69	0.07	14.10	17.80	2.18	0.00	0.11	87.30	7.10	44.00	48.90	3.20
	mantle-1	51.70	0.93	7.73	0.35	3.71	0.11	14.30	17.80	2.35	0.01	0.06	87.40	7.10	43.80	49.20	3.00
	rim-1	50.40	1.83	3.12	0.64	4.87	0.20	16.90	19.00	0.41	0.00	0.06	86.20	8.20	40.90	50.90	12.00
	core-2	51.20	0.93	7.70	0.46	3.72	0.10	14.60	17.90	2.26	0.00	0.04	87.60	7.00	43.50	49.50	3.90
	mantle-2	50.70	0.94	7.89	0.43	3.77	0.10	14.40	17.60	2.11	0.02	0.03	87.30	7.20	43.30	49.50	3.50
	rim-2	50.30	1.02	4.71	0.67	3.84	0.11	16.90	19.80	0.34	0.00	0.03	88.80	6.40	42.50	51.00	8.70
	core-3	50.70	0.89	7.83	0.40	3.65	0.07	14.10	18.20	2.14	0.00	0.04	87.40	7.00	44.70	48.30	3.30
	mantle-3	50.60	0.97	7.90	0.36	3.71	0.09	14.20	18.40	2.34	0.00	0.05	87.30	7.00	44.60	48.40	3.00
rim-3	51.50	1.37	2.08	0.50	4.36	0.19	17.50	20.10	0.24	0.00	0.04	87.90	7.10	41.80	51.10	13.80	
JSB10-27	core-1	50.80	0.95	7.63	0.47	3.89	0.06	14.00	18.30	2.22	0.01	0.07	86.60	7.40	44.70	47.90	4.00
	mantle-1	51.30	0.97	7.83	0.48	3.94	0.10	14.20	18.10	2.24	0.00	0.03	86.60	7.50	44.20	48.40	4.00
	rim-1	50.60	0.91	4.56	0.69	3.62	0.08	15.90	21.60	0.51	0.00	0.05	88.80	6.00	46.20	47.80	9.20

Table 4. The major element composition of olivine (Ol) in the websterite determined by EMPA.

	Position-Particle	SiO ₂	TiO ₂	Al ₂ O ₃	Cr ₂ O ₃	FeO	MnO	MgO	CaO	Na ₂ O	K ₂ O	NiO	Mg [#]
JSB10-43	core-1	40.80	0.03	0.00	0.02	9.99	0.15	48.70	0.05	0.01	0.00	0.39	89.80
	mantle-1	40.60	0.00	0.00	0.06	10.40	0.14	48.60	0.04	0.00	0.02	0.39	89.40
	rim-1	41.30	0.00	0.00	0.01	10.10	0.17	49.40	0.13	0.00	0.00	0.38	89.80
	core-2	40.40	0.00	0.00	0.01	10.40	0.15	48.40	0.05	0.02	0.00	0.45	89.30
	mantle-2	40.70	0.00	0.00	0.01	10.30	0.17	48.90	0.06	0.00	0.00	0.41	89.50
	rim-2	40.50	0.00	0.03	0.15	10.50	0.17	48.30	0.07	0.05	0.00	0.36	89.20
JSB10-47	core	40.40	0.02	0.00	0.04	11.70	0.21	47.00	0.02	0.07	0.00	0.42	87.80
	mantle	40.40	0.01	0.04	0.00	11.60	0.14	47.10	0.03	0.02	0.00	0.39	88.00
	rim	40.60	0.00	0.00	0.09	12.00	0.13	46.60	0.07	0.04	0.02	0.37	87.50
JSB10-02	core	40.90	0.06	0.02	0.01	11.00	0.12	47.10	0.10	0.00	0.00	0.39	88.50
	rim	40.20	0.00	0.02	0.00	12.90	0.36	46.00	0.09	0.00	0.01	0.22	86.50
JSB10-19	core-1	40.00	0.05	0.04	0.00	11.10	0.17	46.80	0.04	0.03	0.00	0.37	88.40
	rim-1	39.90	0.00	0.00	0.03	12.60	0.28	46.40	0.15	0.00	0.00	0.18	86.90
	core-2	40.60	0.05	0.02	0.00	11.60	0.15	47.10	0.09	0.00	0.00	0.32	87.90
	rim-2	40.80	0.08	0.00	0.00	12.50	0.16	47.00	0.13	0.00	0.01	0.14	87.10
	core-3	39.70	0.00	0.05	0.04	11.20	0.13	46.70	0.08	0.00	0.01	0.40	88.30
	rim-3	39.30	0.00	0.00	0.05	13.30	0.21	45.20	0.11	0.00	0.00	0.28	85.90
	core-4	41.60	0.01	0.00	0.01	10.80	0.13	46.00	0.08	0.00	0.00	0.33	88.50
	rim-4	40.30	0.00	0.03	0.02	13.30	0.18	46.00	0.12	0.03	0.01	0.29	86.20
JSB10-31	core-1	40.00	0.02	0.00	0.02	12.20	0.15	46.40	0.08	0.00	0.00	0.40	87.20
	mantle-1	40.10	0.00	0.00	0.02	12.30	0.16	46.60	0.10	0.00	0.01	0.40	87.30
	rim-1	39.80	0.03	0.01	0.06	12.90	0.15	46.50	0.12	0.00	0.02	0.35	86.60
	core-2	40.10	0.00	0.04	0.00	12.20	0.18	46.70	0.10	0.00	0.00	0.36	87.30
	mantle-2	40.00	0.03	0.03	0.04	12.30	0.12	46.70	0.09	0.00	0.00	0.42	87.20
	rim-2	40.20	0.02	0.00	0.00	12.70	0.20	47.30	0.10	0.06	0.00	0.35	87.00
	core-3	39.90	0.00	0.02	0.00	11.80	0.17	47.20	0.08	0.04	0.00	0.35	87.80
	mantle-3	40.60	0.00	0.01	0.07	12.30	0.15	46.60	0.08	0.00	0.01	0.41	87.20
	rim-3	40.40	0.00	0.02	0.01	13.90	0.25	46.10	0.13	0.00	0.01	0.21	85.70

Table 4. Cont.

	Position-Particle	SiO ₂	TiO ₂	Al ₂ O ₃	Cr ₂ O ₃	FeO	MnO	MgO	CaO	Na ₂ O	K ₂ O	NiO	Mg [#]
JSB10-24	core-1	40.20	0.00	0.04	0.05	11.50	0.10	46.80	0.06	0.03	0.00	0.30	88.00
	rim-1	40.40	0.00	0.02	0.02	12.20	0.17	45.60	0.07	0.00	0.01	0.29	87.10
	core-2	39.30	0.00	0.04	0.00	11.00	0.12	46.40	0.09	0.00	0.00	0.35	88.30
	rim-2	39.60	0.00	0.03	0.06	13.10	0.26	45.40	0.08	0.01	0.01	0.21	86.20
JSB10-27	core-1	40.00	0.04	0.01	0.00	12.80	0.11	46.80	0.09	0.07	0.00	0.37	86.80
	mantle-1	39.90	0.02	0.00	0.00	12.90	0.18	46.10	0.06	0.06	0.00	0.37	86.50
	rim-1	38.90	0.01	0.06	0.06	15.30	0.21	44.90	0.17	0.02	0.01	0.22	84.10
	core-2	39.90	0.00	0.02	0.03	12.70	0.14	46.80	0.10	0.00	0.00	0.38	86.90
	mantle-2	39.50	0.04	0.05	0.00	12.70	0.15	46.70	0.06	0.00	0.03	0.39	86.90
	rim-2	40.30	0.01	0.07	0.01	13.70	0.17	46.20	0.09	0.00	0.00	0.39	85.90
JSB10-13-1	core-1	40.40	0.03	0.01	0.00	13.00	0.17	45.70	0.10	0.00	0.00	0.34	86.30
	rim-1	40.30	0.05	0.00	0.00	14.20	0.18	44.80	0.09	0.03	0.00	0.24	85.00
	core-2	39.20	0.00	0.02	0.00	12.80	0.17	45.30	0.06	0.00	0.00	0.32	86.40
	rim-2	39.50	0.02	0.03	0.04	14.70	0.21	43.90	0.07	0.00	0.00	0.30	84.30
JSB10-16	core-1	38.90	0.00	0.04	0.04	10.90	0.15	46.50	0.11	0.07	0.00	0.29	88.50
	rim-1	39.70	0.06	0.02	0.02	12.80	0.22	45.40	0.09	0.03	0.00	0.30	86.50
	core-2	40.40	0.01	0.01	0.01	10.90	0.07	47.20	0.13	0.01	0.00	0.28	88.60
	rim-2	40.10	0.03	0.00	0.01	12.40	0.22	45.80	0.14	0.00	0.00	0.20	86.90

Table 5. The major element composition of spinel (Sp) in the websterite determined by EMPA.

Sample	Position-Particle	SiO ₂	TiO ₂	Al ₂ O ₃	Cr ₂ O ₃	FeO	MnO	MgO	CaO	Na ₂ O	K ₂ O	NiO	Total	Mg [#]	Cr [#]
JSB10-43	core-1	0.00	0.39	39.20	26.90	15.40	0.15	16.60	0.04	0.00	0.00	0.24	98.80	65.90	47.00
	mantle-1	0.00	0.39	39.90	26.80	15.60	0.13	16.70	0.03	0.00	0.00	0.31	99.90	65.90	46.50
	rim-1	0.00	0.35	41.60	26.80	13.70	0.11	17.30	0.01	0.00	0.02	0.23	100.20	69.50	45.40
	core-2	0.00	0.42	40.50	27.00	15.60	0.12	17.20	0.01	0.04	0.00	0.27	101.30	66.40	46.30
	mantle-2	0.00	0.32	39.80	26.30	15.30	0.14	16.80	0.01	0.00	0.00	0.21	98.80	66.30	46.10
	rim-2	0.00	0.39	39.90	26.20	15.00	0.15	16.50	0.00	0.00	0.00	0.25	98.20	66.40	45.90
JSB10-47	core	0.00	0.06	57.40	8.34	12.40	0.12	19.10	0.00	0.00	0.00	0.45	97.90	73.60	15.80
	mantle	0.00	0.12	57.30	8.77	13.20	0.13	19.10	0.01	0.01	0.01	0.43	99.00	72.30	16.50
	rim	0.32	1.06	54.20	9.01	15.40	0.11	18.20	0.14	0.10	0.03	0.37	99.00	68.00	17.70

Table 5. Cont.

Sample	Position-Particle	SiO ₂	TiO ₂	Al ₂ O ₃	Cr ₂ O ₃	FeO	MnO	MgO	CaO	Na ₂ O	K ₂ O	NiO	Total	Mg [#]	Cr [#]
JSB10-02	core-1	0.00	0.20	60.90	6.22	11.50	0.09	20.20	0.02	0.04	0.01	0.41	99.60	76.00	11.70
	core-2	0.00	0.23	60.50	6.37	11.70	0.06	20.00	0.04	0.20	0.00	0.44	99.50	75.60	12.00
	rim-2	0.00	0.20	61.20	6.35	11.30	0.23	19.00	0.05	0.00	0.01	0.20	98.60	75.20	11.80
JSB10-19	core-1	0.00	0.17	60.00	6.51	11.50	0.07	20.00	0.00	0.01	0.00	0.42	98.70	75.70	12.30
	rim-1	0.00	0.21	60.20	6.50	11.10	0.12	19.30	0.01	0.00	0.01	0.34	97.70	75.80	12.30
	core-2	0.00	0.27	59.90	6.53	11.80	0.17	19.20	0.00	0.02	0.00	0.42	98.30	74.40	12.40
	rim-2	0.00	0.18	60.50	6.47	11.90	0.23	18.70	0.00	0.01	0.01	0.16	98.10	74.00	12.10
JSB10-24	core-1	0.00	0.20	59.60	6.13	11.60	0.08	19.90	0.02	0.00	0.00	0.38	97.90	75.50	11.70
	rim-1	0.00	0.17	61.70	6.08	12.00	0.20	18.70	0.00	0.00	0.00	0.29	99.20	73.70	11.30
	core-2	0.00	0.23	59.80	6.17	11.40	0.09	19.70	0.00	0.00	0.01	0.38	97.80	75.80	11.80
	rim-2	0.00	0.20	61.30	6.36	11.30	0.21	19.10	0.07	0.06	0.00	0.24	98.80	75.10	11.80
JSB10-31	core-1	0.02	0.23	59.10	6.41	12.60	0.09	20.40	0.02	0.02	0.00	0.45	99.30	74.30	12.30
	mantle-1	0.01	0.25	58.80	6.50	12.70	0.17	19.60	0.00	0.00	0.01	0.39	98.40	73.50	12.50
	core-2	0.00	0.28	59.40	6.36	12.80	0.20	19.20	0.05	0.04	0.00	0.40	98.70	73.10	12.20
	mantle-2	0.00	0.26	59.60	6.66	13.10	0.27	18.60	0.01	0.00	0.00	0.27	98.70	71.90	12.60
	core-1	0.00	0.24	58.60	6.38	13.30	0.10	20.40	0.01	0.03	0.00	0.49	99.50	73.30	12.30
	rim-1	0.00	0.25	59.10	6.04	12.90	0.20	18.90	0.02	0.00	0.00	0.45	97.90	72.60	11.70
	core-2	0.00	0.27	58.10	6.59	13.40	0.08	20.00	0.00	0.00	0.02	0.46	99.00	72.80	12.80
	mantle-2	0.00	0.29	61.00	6.18	12.90	0.18	19.30	0.05	0.00	0.00	0.38	100.40	73.00	11.60
	core-1	0.02	0.28	58.90	7.15	14.10	0.12	19.20	0.00	0.00	0.00	0.40	100.10	71.00	13.60
	rim-1	0.00	0.15	60.00	6.83	14.20	0.19	17.60	0.02	0.01	0.00	0.30	99.40	69.10	12.80
	core-2	0.00	0.14	58.80	6.78	14.00	0.08	19.30	0.03	0.03	0.01	0.37	99.50	71.20	13.00
rim-2	0.00	0.30	60.30	6.71	12.50	0.09	19.10	0.00	0.04	0.01	0.40	99.40	73.40	12.60	

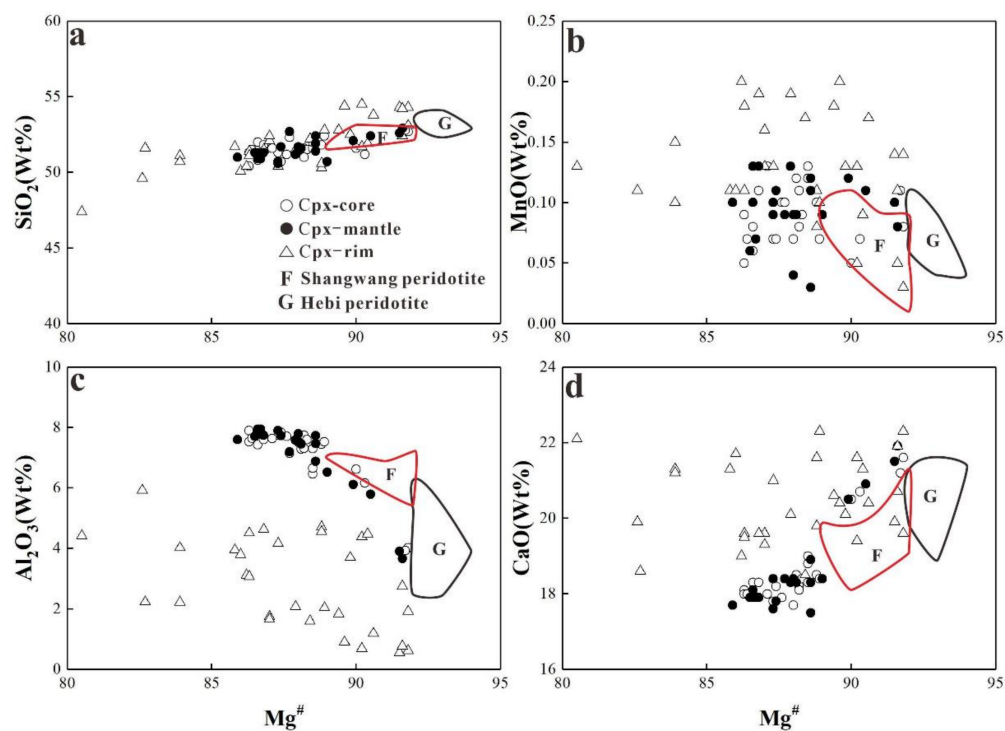


Figure 9. Plots of $Mg^{\#}$ vs. SiO_2 (a), MnO (b), Al_2O_3 (c), and CaO (d) for the clinopyroxene (Cpx) in the websterite. Note: The data of Shanwang and Hebi peridotite are the same as Figure 7.

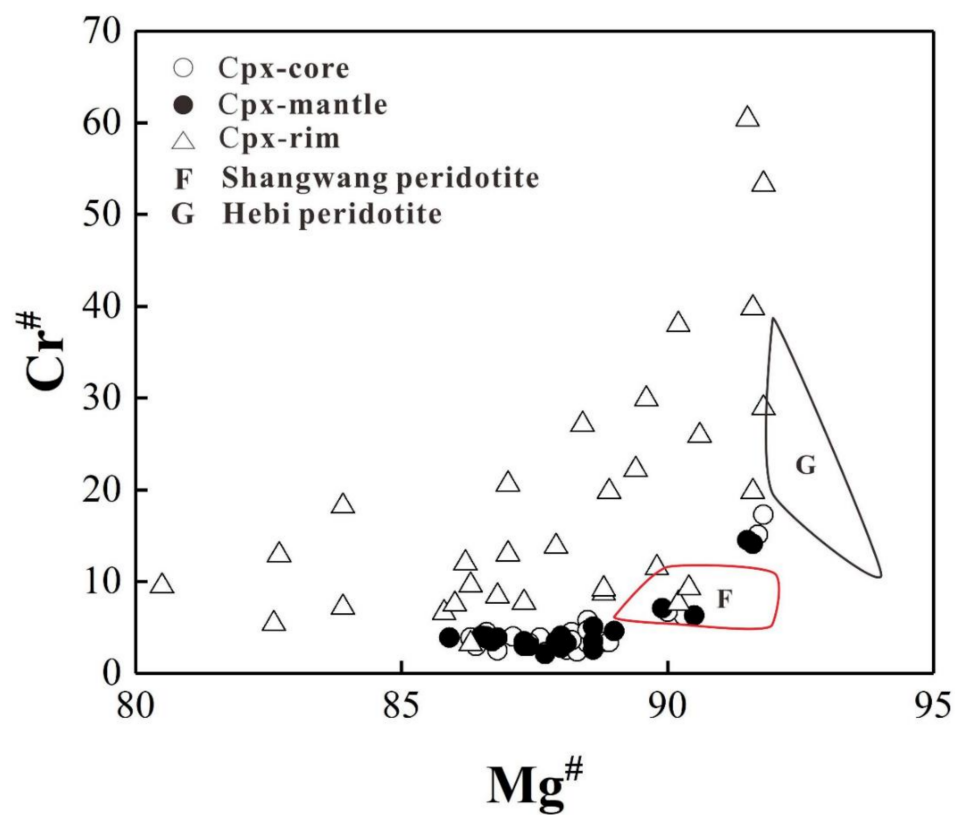


Figure 10. Plots of $Mg^{\#}$ - $Cr^{\#}$ for the clinopyroxene (Cpx) in the websterite. Note: The data of Shanwang and Hebi peridotite are the same as Figure 7.

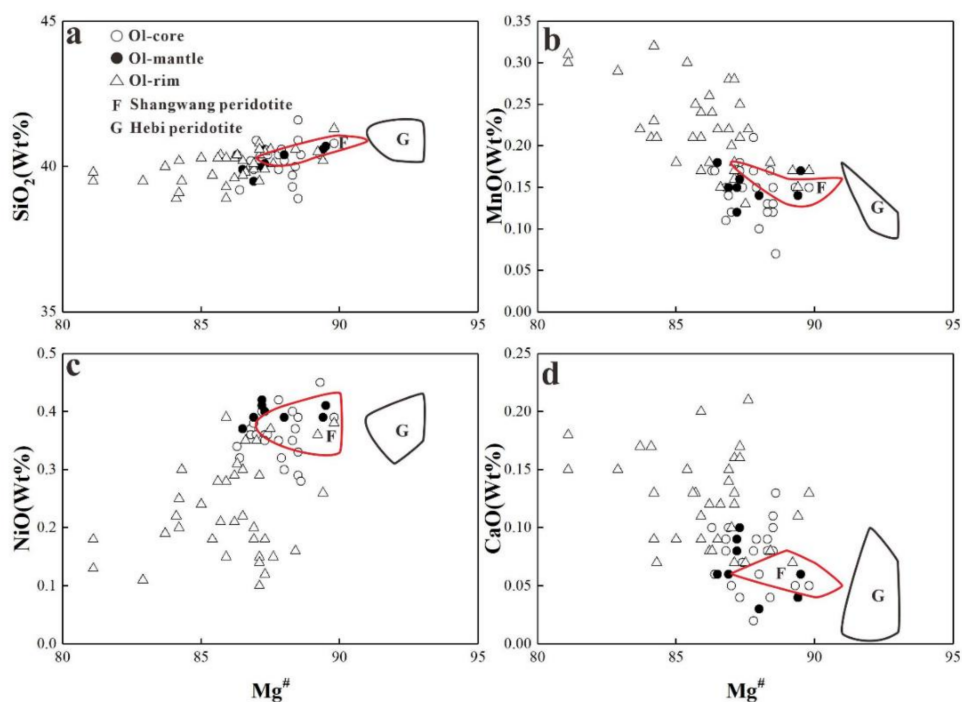


Figure 11. Plots of Mg[#] vs. SiO₂ (a), MnO (b), NiO (c), and CaO (d) for the olivine (Ol). Note: The data of Shanwang and Hebi peridotite are the same as Figure 7.

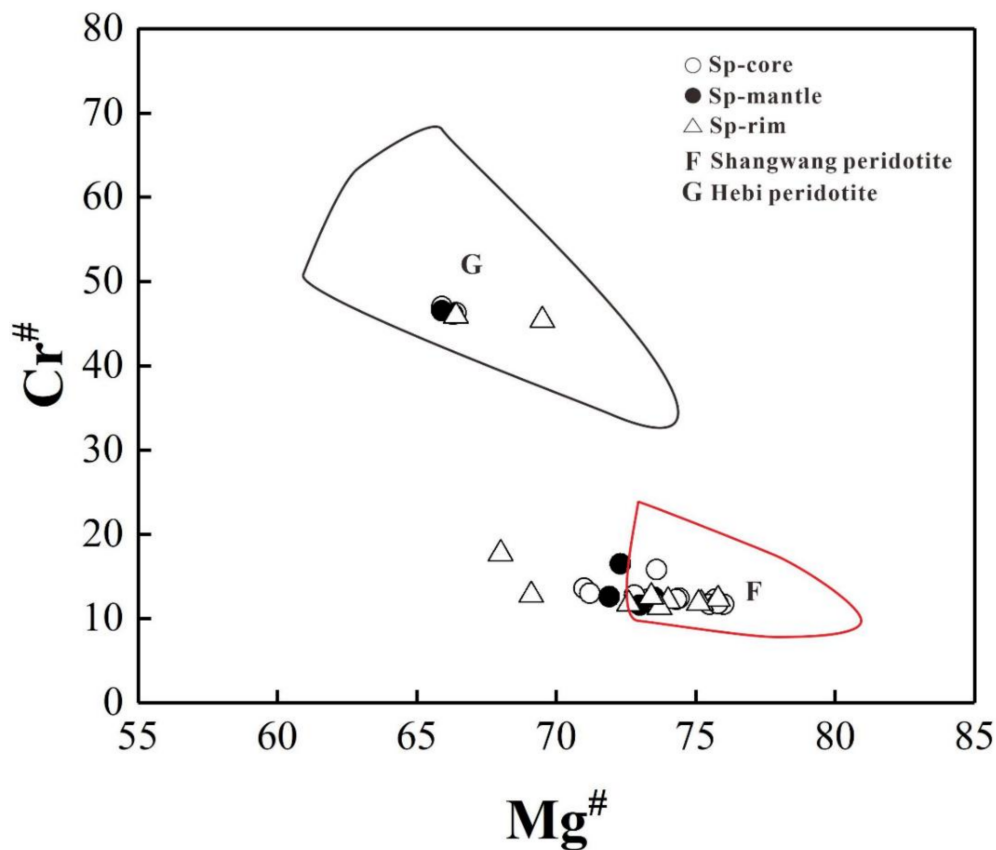


Figure 12. Plots of Mg[#]-Cr[#] for the Spinel (Sp). Note: The data of Shanwang and Hebi peridotite are the same as Figure 7.

4.2.1. Orthopyroxene (Opx)

Most of Opx have En-Fs-Wo contents of En = 78.93–89.50, Fs = 10.62–17.21, Wo = 0.87–4.35, falling into the field of clinoenstatite, whereas a few falls in the pigeonite field (Figure 7). The major element compositions in the core are the same as those in the mantle, but distinct from those in the rim. The cores in most of the samples have high Mg[#] (Mg[#] = 87.0–91.5), while the rims show relatively low Mg[#] (Mg[#] = 82.2–91.3), indicating that the Opx studied mostly have obvious core-rim zoning (Figure 8). In addition, Mg[#] is positively correlated with SiO₂, but negatively correlated with MnO, Al₂O₃, CaO, similar to the trend represented by with the oxides of lherzolite. Figure 7 shows that most of the core and mantle of Opx studied fall in the field of the peridotites from Shanwang [41]. However, no samples fall in the field of the peridotite from Hebi [15].

4.2.2. Clinopyroxene (Cpx)

Cpx have the En-Fs-Wo contents of En = 41.20–54.36, Fs = 4.29–10.45, Wo = 39.46–48.81, falling in the field of augite (Figure 7). Similar to the case of Opx, the core and mantle of Cpx have the same compositions, but their compositions are distinct from those of the rim, indicating obvious core-rim zoning. Generally, Mg[#] in the core of Cpx (Mg[#] = 86.3–91.8) are higher than those in the rim of Cpx (Mg[#] = 80.5–91.8) (Figure 8). Mg[#] is positively correlated with Cr[#], SiO₂ and CaO, but negatively with Al₂O₃ (Figures 9 and 10). Figure 10 shows small variation in Mg[#] and Cr[#] of the core and mantle, but wide ranges of Mg[#] and Cr[#] in the rim. The large variation in Cr[#] of Cpx from Hannuoba peridotites implies that the lithospheric mantle beneath Hannuoba may have experienced different degrees of melting extraction [45].

4.2.3. Olivine (Ol)

As the Ol with a magmatic origin has CaO > 0.1 wt%, and the post-melting mantle residual Ol shows CaO < 0.1 wt%, the content of CaO in Ol can well indicate the genesis of olivine. The compositions of the Ol cores studied almost fall in the field of mantle peridotite, indicating that olivine may be remnants from mantle peridotite (Figure 11). Ol also shows obvious core-rim reaction structures, with exception of only a few samples characterized by the same core and rim composition. The Mg[#] of Ol is relatively low (<90), indicating that the fertile lithospheric mantle represented by websterite. Mg[#] has a weak positive correlation with SiO₂ and a good positive correlation with NiO, but has a negative correlation with MnO and CaO, implying the occurrence of mantle metasomatism. The comparison of the Shanwang and Hebi peridotite data shows that most of the data studied fall in the field of Shanwang peridotite (Figure 11), suggesting that the lithospheric mantle represented by websterite may be newly accreted.

4.2.4. Spinel (Sp)

Sp in the websterite have no obvious core-rim zoning but shows wide ranges of Mg[#] (65.89–75.96) and Cr[#] values (11.29–46.97) (Figure 12). In the figure of Mg[#] vs. Cr[#], most of the samples fall in the field of juvenile mantle represented by the peridotite from Shanwang region, whereas a few samples fall in the field of ancient mantle represented by the peridotite from Hebi (Figure 12).

4.3. Equilibrium Temperature and Pressure of Websterite

The calculated results of the equilibrium temperature and pressure of the websterites studied are shown in Table 6, suggesting that the formation temperature and pressure of the websterite from Hannuoba fall in the range of 1000–1100 °C, and 13–26 kbar (corresponding to the depth of 43–82 km, [46]), respectively.

Table 6. Comparison of different temperatures and geobarometers.

Author T and P	Wells, 1977	Wood and Banno, 1973	Brey and Kohler, 1990
Temperature range/°C	825–1189	934–1178	1074–1121
Average temperature/°C	1004	1074	1091
Pressure range/kbar			14.8–25.7
Average pressure/kbar			21.6

D (depth, its unit is Km) = 4.02 + 3.03 P (pressure, its unit is kbar) (Ave'Lallemant et al. [46]).

5. Discussion

5.1. Mantle Source of the Websterite

The equilibrium temperature and pressure data (Table 6) of the websterite from Hannuoba indicate that the websterite originated from the mantle. As shown in the Harker diagram of major element composition (Figure 4), most of the samples studied fall in the field of the Cenozoic composite pyroxenite, suggesting that the websterite is derived from a newly accreted fertile lithospheric mantle. It is worth noting that some samples fall in the field of the residual Archean lithospheric mantle, indicating that the ancient and juvenile lithospheric mantle coexists beneath Hannuoba. The REE distribution pattern diagram of Hannuoba websterite (Figure 6) shows that there is a large variation in the total content of REE (Σ REE = 9.66–67.28 ppm), and considerable enrichment of LREE in some samples. Furthermore, as shown in the mantle-normalized trace element diagram (Figure 5), most samples are relatively depleted in high field strength elements (HFSEs). These, altogether, suggest that the mantle source of websterite may be contaminated by different degrees of materials from the crust. On the other hand, the websterites have high Nb/Ta ratio (11.36–20.57), implying that the Ti minerals (e.g., rutile) may be involved in the source of the websterite.

5.2. Genesis of the Websterite

The websterite, as an important component of mantle rocks, can provide an important window for unraveling the formation and evolution of lithospheric mantle. There are mainly several models to interpret the genesis of websterite shown as follows: (1) formed by high-pressure fractional crystallization of basaltic magmas during magma ascent through the mantle channel. The resulted rocks were considered to be characterized by upward inverted "U" curve of REE, with obvious enrichment of Eu [39,40,47,48]; (2) originated from reaction of peridotite with silica-rich melts derived from the recycled oceanic crust or subducted lower continental crust, which results in the formation of minerals such as Opx and even Cpx [32,34,49,50]; (3) derived from the solidification of infiltrating magmas or in-situ crystallization of peridotitic melts [28,47,51,52]; (4) produced as a part of the sub-continental lithospheric mantle by high-pressure metamorphism of the gabbros from subducted oceanic crust or the basaltic cumulate rocks. These kinds of rocks produced are mainly characterized by distinctly positive Eu anomaly [53–55]; (5) directly sourced from residual mantle [56,57].

The major elemental compositions of the websterites studied are obviously different from those of the pyroxenites with the global cumulate origin (Figure 4). On the one hand, the Mg[#], TiO₂ and Na₂O contents of most samples studied are significantly higher than those of the pyroxenite. On the other hand, the REE distribution patterns of the websterites almost show weak depletion rather than upward-inverted "U" enrichment (Figure 6) pattern. Therefore, the cumulate origin of the websterites can be excluded. This can be also evidenced by the formation pressure of the websterites (12–26 kbar) (Table 6). Depletion of the HFSEs (e.g., Zr, Hf) in the websterite indicates that the pyroxenite are not formed by the high-pressure fractional crystallization of the melts during the magma ascent through the mantle channel. The Eu in the websterites do not show distinctly positive anomaly, suggesting that pyroxenite is also not metamorphosed from subducted oceanic crust. The trace element distribution patterns of the websterites are distinct from those of

the Paleozoic garnet pyroxenites that represent the melt crystallization. Some of the major elements in the websterites fall into the field of the residual Archean lithospheric mantle, and some data fall in the field of Hannuoba Cr-pyroxenite that represents the residual mantle through different degrees of melting; the basaltic components (e.g., Al_2O_3 and CaO) are negatively correlated with $\text{Mg}^\#$. These altogether suggest that the websterites inherit part of the geochemical characteristics of residual mantle. This is also demonstrated by the major element covariance diagram of $\text{Mg}^\#$ vs. oxides of Opx and Cpx in the websterites (Figures 8 and 9). However, the trace element characteristics of the websterites cannot be produced from a single residual mantle source. Therefore, Hannuoba websterite is more likely to be produced by the interaction between the ancient residual mantle peridotite and the late-stage melts, as evidenced by the following points: (1) The CaO content of the Ol in the websterite is less than 0.1%, and that in the core almost fall into the field of mantle peridotite, indicating that the Ol is probably the residual Ol of mantle peridotite; in addition, most of the whole rock data fall into the field of the Cenozoic composite pyroxenite formed by interaction, suggesting that the formation of the websterite is closely related to peridotite-melt interaction; (2) The typical minerals of websterite xenoliths, such as olivine, orthopyroxene, and clinopyroxene, mostly have core-rim reaction structures, demonstrating that the metasomatic melts might be involved in the source. Positive correlation of $\text{Mg}^\#$ with SiO_2 and NiO , but negative correlation with MnO and CaO may suggest the metasomatism. It is worth noting that $\text{Mg}^\#$ and NiO in the rim of Ol lower than those in the core, but MnO in the former higher than the latter may be related to the imbalance of peridotite-melt reaction or the impact of post-metasomatism; (3) The Al_2O_3 and CaO of the websterites decrease with the MgO implies that the formation of the websterites may be the incorporated effects of partial melting of the ancient lithospheric mantle and peridotite-melt reaction [11], which is also demonstrated by the good correlation of $\text{Mg}^\#$ vs. MnO , Al_2O_3 , CaO and NiO of Opx, Cpx, and Ol.

5.3. Source and Characteristics of Metasomatic Melt

As mentioned above, mantle metasomatism [58] (or melt-peridotite interaction) is the key point for the formation of Hannuoba websterites. Mantle metasomatism can be generally divided into three types: (1) Concealed metasomatism: the mineral composition changes with the formation of new minerals during the metasomatism, e.g., Ol reacts with melt 1 to form Cpx and melt 2, with $\text{Mg}^\#$ decrease in the residual olivine [59]; (2) Apparent metasomatism: typical volatile-bearing minerals such as phlogopite and hornblende are formed during this metasomatism [60]; (3) Cryptic metasomatism: no characteristic metasomatic minerals are formed, with only change in the compositions of the minerals or whole rocks during metasomatism [61]. In this study, the mineral assemblage of websterite is $\text{Ol} + \text{Opx} + \text{Cpx} + \text{Sp} \pm \text{Grt}$, with the main minerals of Cpx and Opx, and the minor minerals as Ol, indicating that the mantle metasomatism beneath Hannuoba belongs to the concealed metasomatism.

The melts involved in the mantle metasomatism are divided into silicic melts and carbonatic melts [62]. Carbonatite melts are characterized by the depletion of Si, Al, Ti, Ga, and Zr, enrichment of REEs, and high $(\text{La}/\text{Yb})_N$ [63]. Their reaction with peridotites, shown as carbonatite melts + Opx = Cpx + Ol + melts, can transform harzburgites or lherzolites into Cpx-rich peridotites or websterite [64], consequently resulting in the transformation of the refractory and depleted (depleted in Cpx and LREEs) mantle into fertile and enriched mantle (rich in Cpx and LREEs). However, carbonatite melts that react with metasomatic mantle peridotite cannot produce the petrographic characteristics of the websterite observed in this study. Furthermore, all the websterites studied fall into the metasomatic field of silicate melts (Figure 13), consistent with the case of Cenozoic composite pyroxenites [38]. Therefore, it is suggested that the websterite from Hannuoba is formed by the interaction between mantle peridotite and silica-rich melts.

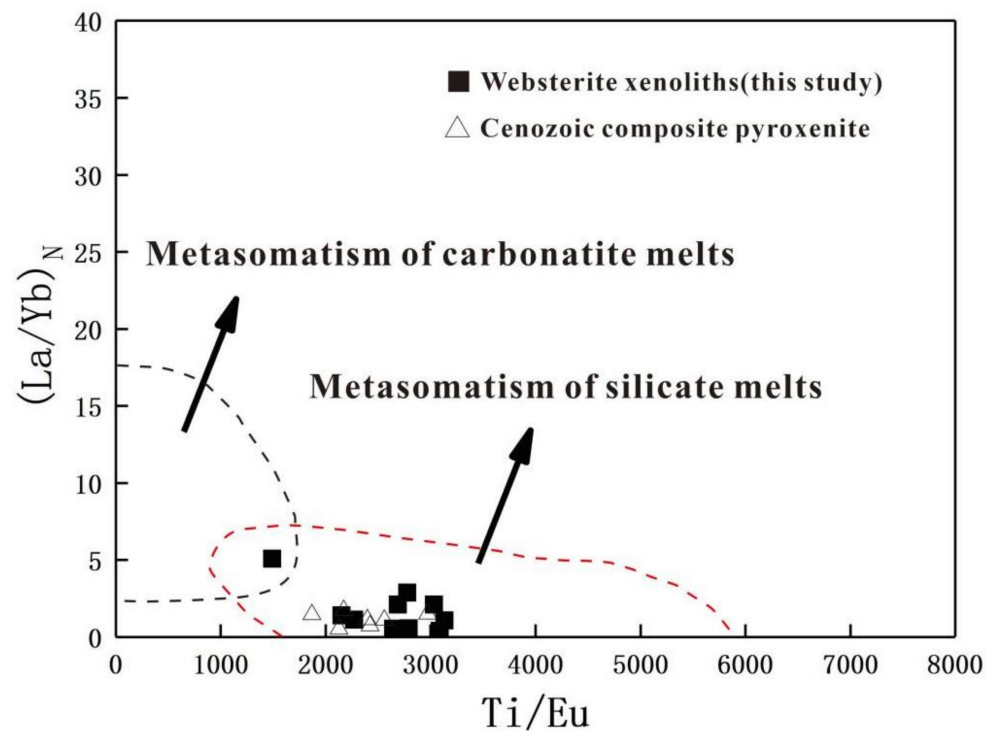


Figure 13. Discrimination diagram of metasomatism. Note: Cenozoic composite pyroxenite data are sourced from Liu et al. [38]).

Silica-rich melts include the following source of melts: (1) Asthenosphere-derived melts whose interaction with the peridotite can result in enrichment of mantle peridotites, with a decrease in refractory components and an increase in fusible components; (2) The melts originated from subducted crustal plate, whose interaction with peridotites and melts can form harzburgites or websterite and cause the enrichment of the refractory and depleted lithospheric mantle.

In the Harker diagram of major elements in the whole rocks (Figure 4), the fusible basaltic components such as Al_2O_3 and CaO decrease with $Mg^\#$, which can be interpreted as a result of a two-stage process, that is, the websterite may be formed following the incorporated trends of partial melting (residual mantle peridotite formed by high-degree melting) and interaction (interaction of asthenosphere-derived basaltic melt with peridotite) [11], suggesting that the metasomatic melts may be mainly asthenosphere-derived basaltic melts, as also evidenced by the OIB-type geochemical characteristics of the websterites (Figure 5). This is consistent with the point suggested by the previous studies [65,66]. The REE and trace element patterns of the websterite show a large variation in ΣREE , LREEs, and HREEs ($\Sigma REE = 9.66\text{--}67.28$ ppm, LREE = 5.1–57.28 ppm, HREE = 2.37–16.79 ppm), and enrichment in LREEs, LILEs (e.g., Rb, Ba, U, Pb, Sr), and depletion in HFSE (e.g., Zr, Hf, Nb, Ta) in some samples (Table 1, Figure 6), suggesting that the crustal materials are probably involved in the source.

5.4. Implication for Destruction of North China Craton

The North China Craton remained stable up to Paleozoic. However, strong activation that took place in the North China Craton (especially in the eastern part) during Mesozoic and Cenozoic not only thinned the ancient and thick lithospheric mantle by more than 100 km, but also drastically transformed the physical and chemical properties of the lithospheric mantle beneath the North China Craton. This process is also known as “destruction”. Pyroxenite, though less in the mantle, plays an important role in the formation and evolution of the mantle. The websterites from Hannuoba are the products of the interaction between the silica-rich melts and the lherzolites formed by the partial

melting of the ancient residual mantle. These silica-rich melts are mainly derived from the asthenospheric mantle, with involvement of crustal materials. The interaction between silica-rich melts and mantle peridotite can transform an ancient and refractory mantle into a newly accreted and fertile lithospheric mantle, thus resulting in the destruction of the North China Craton.

Previous studies suggested that the Paleo-Pacific plate subducted toward the lithospheric mantle beneath eastern China since the Jurassic [67–69]. This implies that the crustal melts that interact with the mantle may be derived from the subducted Paleo-Pacific plate. The interaction between the lithospheric mantle and the melts released from the subducted oceanic plate can significantly transform the physico-chemical properties of the lithospheric mantle. This implies that the subduction of the Paleo-Pacific plate may play an important role in the destruction of the North China Craton.

6. Conclusions

Based on the petrological, mineralogical, and geochemical studies of the Ol websterite xenoliths entrapped in the Cenozoic basalts from Hannuoba, NCC, the following conclusions can be drawn:

(1) The source of the websterite is mainly the newly accreted lithospheric mantle, which may be contaminated by different degrees of crustal materials; in addition, a small amount of residual ancient lithospheric mantle may be involved in the source. The high Nb/Ta ratios of the websterites indicate that the source may be affected by Ti-bearing minerals (e.g., rutile);

(2) The websterite is mainly produced by the interaction between mantle peridotite and silica-rich melts. These melts are mainly derived from the asthenospheric mantle, with small involvement of crustal materials;

(3) The metasomatic crustal melts may be derived from the subducted Paleo-Pacific plate. These melts interacted with the lithospheric mantle can significantly change the chemical composition of the lithospheric mantle, and consequently result in the destruction of the North China Craton.

Author Contributions: Conceptualization, X.D., P.F. and Z.T.; methodology, X.D.; validation, X.D., H.S., N.L., W.X., P.F. and Z.T.; data curation, X.D., H.S., Q.S. and H.H.; writing—original draft preparation, X.D., H.S., N.L., W.X., Q.S., H.H., P.F. and Z.T.; writing—review and editing, X.D., H.S., Q.S., H.H., P.F. and Z.T. All authors have read and agreed to the published version of the manuscript.

Funding: This work was financially supported by National Natural Science Foundation (42102060, 42003028), China Postdoctoral Science Foundation (2021M692983), Talent foundations of University of South China (2014XQD08; 2018XQD22), and Innovative Training Program of University of South China (X2019098).

Data Availability Statement: All data generated or used during the study appear in the submitted article.

Acknowledgments: We appreciate Benxun Su for the major and trace element analysis of mineral and whole rock, and Hongfu Zhang, Xinmao Zhao, and Yan Xiao for the field support. Editor Aleksandar Pavlovic and two anonymous reviewers are much acknowledged for their constructive comments, which greatly helped to strengthen this paper.

Conflicts of Interest: The authors declare no conflict of interest.

References

1. Pearson, D.G. The age of continental roots. *Lithos* **1999**, *48*, 171–194. [[CrossRef](#)]
2. Richardson, S.H.; Gurney, J.J.; Erlank, A.J.; Harris, J.W. Origin of diamonds in old enriched mantle. *Nature* **1984**, *310*, 198–202. [[CrossRef](#)]
3. Richardson, S.H.; Erlank, A.J.; Hart, S.R. Kimberlite-borne garnet peridotite xenoliths from old enriched subcontinental lithosphere. *Earth Planet. Sci. Lett.* **1985**, *75*, 116–128. [[CrossRef](#)]
4. Fan, W.M.; Zhang, H.F.; Baker, J.; Jarvis, K.E.; Mason, P.R.D.; Menzies, M.A. On and off the North China Craton: Where is the Archean keel? *J. Petrol.* **2000**, *41*, 933–950. [[CrossRef](#)]

5. Griffin, W.L.; Zhang, A.; O'Reilly, S.Y.; Ryan, C. Phanerozoic evolution of the lithosphere beneath the Sino-Korean craton. In *Mantle Dynamics and Plate Interaction in East Asia*; Flower, M.F.J., Chung, S.-L., Lo, C.-H., Lee, T.-Y., Eds.; Geodynamics Series; American Geophysical Union: San Francisco, CA, USA, 1998; Volume 27, pp. 107–126.
6. Menzies, M.A.; Fan, W.; Zhang, M. Palaeozoic and Cenozoic lithoprobes and the loss of >120 km of Archaean lithosphere, Sino-Korean craton, China. *Geol. Soc. Lond. Spec. Publ.* **1993**, *76*, 71–81. [[CrossRef](#)]
7. Menzies, M.A.; Xu, Y.G. Geodynamics of the North China craton. In *Mantle Dynamics and Plate Interaction in East Asia*; Flower, M.F.J., Chung, S.-L., Lo, C.-H., Lee, T.-Y., Eds.; Geodynamics Series 27; American Geophysical Union: San Francisco, CA, USA, 1998; Volume 100, pp. 155–164.
8. Xu, Y.G. Thermo-tectonic destruction of the archaean lithospheric keel beneath the Sino-Korean Craton in China: Evidence, timing and mechanism. *Phys. Chem. Earth Part A Solid Earth Geod.* **2001**, *26*, 747–757. [[CrossRef](#)]
9. Ying, J.; Zhang, H.; Kita, N.; Morishita, Y. Nature and evolution of Late Cretaceous lithospheric mantle beneath the eastern North China Craton: Constraints from petrology and geochemistry of peridotitic xenoliths from Jūnan, Shandong Province, China. *Earth Planet. Sci. Lett.* **2006**, *244*, 622–638. [[CrossRef](#)]
10. Zhang, H.F.; Sun, M.; Zhou, X.H.; Fan, W.M.; Zhai, M.; Yin, J.F. Mesozoic lithosphere destruction beneath the North China Craton: Evidence from major-, trace-element and Sr–Nd–Pb isotope studies of Fangcheng basalts. *Contrib. Miner. Petrol.* **2002**, *144*, 241–254. [[CrossRef](#)]
11. Zhang, H.F. Peridotite-melt interaction: A key point for the destruction of cratonic lithospheric mantle. *Chin. Sci. Bull.* **2009**, *54*, 3417–3437. (In Chinese with English Abstract) [[CrossRef](#)]
12. Zhang, H.F. Transformation of lithospheric mantle through peridotite-melt reaction: A case of Sino-Korean craton. *Earth Planet. Sci. Lett.* **2005**, *237*, 768–780. [[CrossRef](#)]
13. Zhang, H.F.; Nakamura, E.; Sun, M.; Kobayashi, K.; Zhang, J.; Ying, J.F.; Tang, Y.J.; Niu, L.F. Transformation of subcontinental lithospheric mantle through peridotite-melt reaction: Evidence from a highly fertile mantle xenolith from the North China craton. *Int. Geo. Rev.* **2007**, *49*, 658–679. [[CrossRef](#)]
14. Zhang, H.F.; Deloule, E.; Tang, Y.J.; Ying, J.F. Melt/rock interaction in remains of refertilized Archean lithospheric mantle in Jiaodong Peninsula, North China Craton: Li isotopic evidence. *Contrib. Miner. Petrol.* **2010**, *160*, 261–277. [[CrossRef](#)]
15. Zheng, J.; O'Reilly, S.Y.; Griffin, W.L.; Lu, F.; Zhang, M.; Pearson, N.J. Relict refractory mantle beneath the eastern North China block: Significance for lithosphere evolution. *Lithos* **2001**, *57*, 43–66. [[CrossRef](#)]
16. Zheng, J.; Griffin, W.L.; O'Reilly, S.Y.; Yang, J.; Li, T.; Zhang, M.; Zhang, R.Y.; Liou, J.G. Mineral Chemistry of Peridotites from Paleozoic, Mesozoic and Cenozoic Lithosphere: Constraints on Mantle Evolution beneath Eastern China. *J. Petrol.* **2006**, *47*, 2233–2256. [[CrossRef](#)]
17. Gao, S.; Rudnick, R.L.; Carlson, R.W.; McDonough, W.F.; Liu, Y.S. Re–Os evidence for replacement of ancient mantle lithosphere beneath the North China craton. *Earth Planet. Sci. Lett.* **2002**, *198*, 307–322. [[CrossRef](#)]
18. Gao, S.; Rudnick, R.L.; Yuan, H.L.; Liu, X.M.; Liu, Y.S.; Xu, W.L.; Ling, W.L.; Ayers, J.C.; Wang, X.C.; Wang, Q.H. Recycling lower continental crust in the North China Craton. *Nature* **2004**, *432*, 892–897. [[CrossRef](#)]
19. Wu, F.Y.; Walker, R.J.; Ren, X.W.; Xun, D.; Zhou, X. Osmium isotopic constraints on the age of lithospheric mantle beneath northeastern China. *Chem. Geol.* **2003**, *196*, 107–129. [[CrossRef](#)]
20. Niu, Y. Generation and Evolution of Basaltic Magmas: Some Basic Concepts and a New View on the Origin of Mesozoic-Cenozoic Basaltic Volcanism in Eastern China. *Geol. J. China Univ.* **2005**, *11*, 9–46.
21. Zhao, G.; Cawood, P.A.; Wilde, S.A.; Sun, M.; Lu, L. Metamorphism of basement rocks in the Central Zone of the North China Craton: Implications for paleoproterozoic tectonic evolution. *Precambrian Res.* **2000**, *103*, 55–88. [[CrossRef](#)]
22. Zhao, G.; Wilde, S.A.; Cawood, P.A.; Sun, M. Archean blocks and their boundaries in the North China Craton: Lithological, geochemical, structural and P-T path constraints and tectonic evolution. *Precambrian Res.* **2001**, *107*, 45–73. [[CrossRef](#)]
23. Zhao, G.; Sun, M.; Wilde, S.A.; Sanzhong, L. Late Archean to paleoproterozoic evolution of the North China Craton: Key issues revisited. *Precambrian Res.* **2005**, *136*, 177–202. [[CrossRef](#)]
24. Zhou, X.; Sun, M.; Zhang, G.; Chen, S. Continental crust and lithosphere mantle interaction beneath North China: Isotopic evidence from granulite xenoliths in Hannuoba, Sino-Korean craton. *Lithos* **2002**, *62*, 111–124. [[CrossRef](#)]
25. Zheng, J.; Lu, F. Mantle xenoliths from kimberlites, Shandong and Liaoning: Paleozoic mantle character and its heterogeneity. *Acta Petrol. Sin.* **1999**, *15*, 65–74. (In Chinese with English Abstract)
26. Yang, J.H.; Wu, F.Y.; Wilde, S.A. A review of the geodynamic setting of large-scale Late Mesozoic gold mineralization in the North China Craton: An association with lithospheric thinning. *Ore Geol. Rev.* **2003**, *23*, 125–152. [[CrossRef](#)]
27. Chen, D.; Zhi, X.; Li, B.; Wang, Y.; Yang, J. Nd, Sr and Pb Isotopic compositions and their petrogenetic information of pyroxenite xenoliths from Hannuoba basalts, China. *Geochimica* **1997**, *26*, 1–11. (In Chinese with English Abstract)
28. Chen, S.; Zhang, G.; Zhou, X.; Sun, M.; Feng, J.; Xie, M. Petrological Investigations on the Granulite Xenoliths from Hannuoba Basalts, Northern Sino-Korean Craton. *Acta Petrol. Sin.* **1998**, *14*, 366–380. (In Chinese with English Abstract)
29. Du, X.; Fan, Q. Discussion on genesis of pyroxenite and granulite xenoliths from Hannuoba. *Acta Petrol. Sin.* **2011**, *27*, 2927–2936. (In Chinese with English Abstract)
30. Fan, Q.; Sui, J.; Liu, R.; Zhou, X. Eclogite facies garnet-pyroxenolite xenolith in Hannuoba area New evidence of magma underplating. *Acta Petrol. Sin.* **2001**, *17*, 1–6. (In Chinese with English Abstract)

31. Zhang, G.; Zhou, X.; Sun, M.; Chen, S.; Feng, J. Sr, Nd and Pb isotopic characteristics of granulite and pyroxenite xenoliths in Hannuoba basalts, Hebei Province, and their implications for geologic processes. *Acta Petrol. Sin.* **1998**, *14*, 190–197. (In Chinese with English Abstract)
32. Zong, K.; Liu, Y.; Gao, S.; Yuan, H.; Liu, X.; Wang, X. In situ trace elemental compositions and geodynamic significance of clinopyroxene in pyroxenite xenoliths from Hannuoba. *Acta Petrol. Sin.* **2005**, *21*, 909–920. (In Chinese with English Abstract)
33. Hirschmann, M.M.; Kogiso, T.; Baker, M.B.; Stolper, E.M. Alkalic magmas generated by partial melting of garnet pyroxenite. *Geology* **2003**, *31*, 481–484. [[CrossRef](#)]
34. Sobolev, A.V.; Hofmann, A.W.; Sobolev, S.V.; Nikogosian, I. An olivine-free mantle source of Hawaiian shield basalts. *Nature* **2005**, *434*, 590–597. [[CrossRef](#)] [[PubMed](#)]
35. Hirschmann, M.M.; Stolper, E.M. A possible role for garnet pyroxenite in the origin of the “garnet signature” in MORB. *Contrib. Miner. Petrol.* **1996**, *124*, 185–208. [[CrossRef](#)]
36. Schiano, P.; Eiler, J.M.; Hutcheon, I.D.; Stolper, E.M. Primitive CaO-rich, silica-undersaturated melts in island arcs: Evidence for the involvement of clinopyroxene-rich lithologies in the petrogenesis of arc magmas. *Geochem. Geophys. Geosyst.* **2000**, *1*, 1018–1051. [[CrossRef](#)]
37. Lu, F.; Han, Z.; Zheng, J.; Ren, Y. Characteristics of Paleozoic mantle-lithosphere in Fuxian, Liaoning Province. *Geol. Sci. Technol. Inf.* **1991**, *10*, 2–20. (In Chinese with English Abstract)
38. Liu, Y.; Gao, S.; Lee, C.T.A.; Hu, S.H.; Liu, X.; Yuan, H. Melt–peridotite interactions: Links between garnet pyroxenite and high-Mg[#] signature of continental crust. *Earth Planet. Sci. Lett.* **2005**, *234*, 39–57.
39. Xiong, Q.; Zheng, J.P.; Griffin, W.L.; O’Reilly, S.Y.; Pearson, N.J. Pyroxenite Dykes in Orogenic Peridotite from North Qaidam (NE Tibet, China) Track Metasomatism and Segregation in the Mantle Wedge. *J. Petrol.* **2014**, *55*, 2347–2376. [[CrossRef](#)]
40. Xu, Y.G. Evidence for crustal components in the mantle and constraints on crustal recycling mechanisms: Pyroxenite xenoliths from Hannuoba, North China. *Chem. Geol.* **2002**, *182*, 301–322. [[CrossRef](#)]
41. Zheng, J.; Lu, F.; Cheng, Z.; Zhao, L. Characteristics and Genesis of Pyroxenite Xenolith in Kimberlite. *Earth Sci.-J. China Univ. Geosci.* **1998**, *23*, 49–54. (In Chinese with English Abstract)
42. Zhou, Q.; Xu, W.; Yang, D.; Pei, F.; Wang, W.; Yuan, H.; Gao, S. Modification of lithospheric mantle by melt derived from recycled continental crust evidenced by wehrlite xenoliths in Early Cretaceous high-Mg diorites from western Shandong. *Sci. China Earth Sci.* **2012**, *55*, 1972–1986. (In Chinese with English Abstract) [[CrossRef](#)]
43. Sun, S.-S.; McDonough, W.F. Chemical and isotopic systematics of oceanic basalts: Implications for mantle composition and processes. *Geo. Soc. Lond. Spec. Publ.* **1989**, *42*, 313–345. [[CrossRef](#)]
44. Morimoto, N. Nomenclature of Pyroxenes. *Mineral. Petrol.* **1988**, *39*, 55–76. [[CrossRef](#)]
45. Zheng, J.; Lu, F.; Yu, C.; O’Reilly, S.Y. Mantle Replacement: Evidence from Comparison in Trace Elements between Peridotite and Diopside from Refractory and Fertile Mantle, North China. *Earth Sci.-J. China Univ. Geosci.* **2003**, *28*, 235–240. (In Chinese with English Abstract)
46. Ave’Lallemant, H.G.; Mercier, J.C.; Carter, N.L. Rheology of the upper mantle: Inferences from peridotite xenoliths. *Tectonophysics* **1980**, *70*, 85–113. [[CrossRef](#)]
47. Frey, F.A. The origin of pyroxenites and garnet pyroxenites from Salt Lake Crater, Oahu, Hawaii: Trace element evidence. *Am. J. Sci.* **1980**, *280-A*, 427–449.
48. Huang, X.; Xu, X.; Cai, Y.; Zhou, X. Deep-seated xenoliths in Nushan alkali basalts, Anhui Province. *J. Nanjing Univ. (Nat. Sci.)* **1998**, *34*, 292–301. (In Chinese with English Abstract)
49. Liu, J.F. Nature of Mantle Lithosphere Beneath the Western North China Craton: Constraints from the Mantle Xenoliths in Cenozoic Basalts from Yangyuan, Hebei Province. Ph.D. Thesis, Guangzhou Institute of Geochemistry, Chinese Academy of Science, Guangzhou, China, 2005. (In Chinese with English Abstract)
50. Xu, W.; Zhou, Q.J.; Pei, F.; Yang, D.; Gao, S.; Li, Q.; Yang, Y. Destruction of the North China Craton: Delamination or thermal/chemical erosion? Mineral chemistry and oxygen isotope insights from websterite xenoliths. *Gondwana Res.* **2013**, *23*, 119–129. [[CrossRef](#)]
51. Chen, S.; O’Reilly, S.Y.; Zhou, X.; Griffin, W.L.; Zhang, G.; Sun, M.; Feng, J.; Zhang, M. Thermal and petrological structure of the lithosphere beneath Hannuoba, Sino-Korean Craton, China: Evidence from xenoliths. *Lithos* **2001**, *56*, 267–301. [[CrossRef](#)]
52. Lee, C.T.A. Geochemical/petrologic constraints on the origin of cratonic mantle. *Geophys. Mono* **2006**, *164*, 89–114.
53. Jacob, D.E.; Viljoen, K.S.; Grassineau, N.V. Eclogite xenoliths from Kimberley, South Africa—A case study of mantle metasomatism in eclogites. *Lithos* **2009**, *112*, 1002–1013. [[CrossRef](#)]
54. Morishita, T.; Arai, S.; Gervilla, F.; Green, D.H. Closed-system geochemical recycling of crustal materials in alpine-type peridotite. *Geochim. Cosmochim. Acta* **2003**, *67*, 303–310. [[CrossRef](#)]
55. Yu, S.Y.; Xu, Y.G.; Ma, J.L.; Zheng, Y.F.; Kuang, Y.S.; Hong, L.B.; Ge, W.C.; Tong, L.X. Remnants of oceanic lower crust in the subcontinental lithospheric mantle: Trace element and Sr-Nd-O isotope evidence from aluminous pyroxenite xenoliths from Jiaohe, Northeast China. *Earth Planet. Sci. Lett.* **2010**, *297*, 413–422. [[CrossRef](#)]
56. Jackson, E.D.; Wright, T.L. Xenoliths in the Honolulu Volcanic Series, Hawaii. *J. Petrol.* **1970**, *11*, 405–433. [[CrossRef](#)]
57. White, R.W. Ultramafic inclusions in basaltic rocks from Hawaii. *Contrib. Miner. Petrol.* **1966**, *12*, 245–314. [[CrossRef](#)]
58. Bailey, D.K. Volatile flux, heat focusing and the generation of magma. *Gao J. Spec.* **1970**, *2*, 177–186.

59. Harlov, D.E.; Austrheim, H. Metasomatism and the Chemical Transformation of Rock: Rock-Mineral-Fluid Interaction in Terrestrial and Extraterrestrial Environments. In *Metasomatism and the Chemical Transformation of Rock: The Role of Fluids in Terrestrial and Extraterrestrial Processes*; Springer: Berlin/Heidelberg, Germany, 2013; pp. 1–16.
60. Harte, B. Mantle peridotites and processes: The kimberlite sample. In *Continental Basalts and Their Xenoliths*; Hawkesworth, C.J., Norry, M.J., Eds.; Shiva: Nantwich, UK, 1983; pp. 46–91.
61. Dawson, J.B. Contrasting Types of Upper-Mantle Metasomatism? *Dev. Petrol.* **1984**, *11*, 289–294.
62. Bodinier, J.L.; Menzies, M.; Shimizu, N.; Frey, F.A.; McPherson, E. Silicate, hydrous and carbonate metasomatism at Lherz, France: Contemporaneous derivatives of silicate melt-harzburgite reaction. *J. Petrol.* **2004**, *45*, 299–320. [[CrossRef](#)]
63. Gasparik, T.; Litvin, Y.A. Experimental investigation of the effect of metasomatism by carbonatic melt on the composition and structure of the deep mantle. *Lithos* **2002**, *60*, 129–143. [[CrossRef](#)]
64. Yaxley, G.M.; Crawford, A.J.; Green, D.H. Evidence for Carbonatite Metasomatism in Spinel Peridotite Xenoliths from Western Victoria, Australia. *Earth Planet. Sci. Lett.* **1991**, *107*, 305–317. [[CrossRef](#)]
65. Tang, Y.J.; Zhang, H.F.; Ying, J.F. Asthenosphere-lithospheric interaction in an extensional regime: Implication from the geochemistry of Cenozoic basalts from Taihang Mountains, North China Craton. *Chem. Geol.* **2006**, *233*, 309–327. [[CrossRef](#)]
66. Zhang, H.F.; Sun, Y.L.; Tang, Y.J.; Xiao, Y.; Zhang, W.; Zhao, X.; Santosh, M.; Menzies, M. Melt-peridotite interaction in the Pre-Cambrian mantle beneath the western North China Craton: Petrology, geochemistry and Sr, Nd and Re isotopes. *Lithos* **2012**, *149*, 100–114. [[CrossRef](#)]
67. Zhu, R.; Xu, Y.; Zhu, G.; Zhang, H.; Xia, Q.; Zheng, T. Destruction of the North China Craton. *Sci. China Earth Sci.* **2012**, *55*, 1565–1587. (In Chinese with English Abstract) [[CrossRef](#)]
68. Zhu, R.; Xu, Y. The subduction of the west Pacific plate and the destruction of the North China Craton. *Sci. China Earth Sci.* **2019**, *62*, 1340–1350. (In Chinese with English Abstract) [[CrossRef](#)]
69. Xu, W.L.; Wang, D.Y.; Wang, Q.H.; Lin, J.Q. Petrology and geochemistry of two types of mantle derived xenoliths in Mesozoic diorite from western Shandong Province. *Acta Petrol. Sin.* **2003**, *19*, 623–636. (In Chinese with English Abstract)